Liquid-like dynamics in a solid-state lithium electrolyte

Jingxuan Ding,[1,2] Mayanak K. Gupta,[1,3] Carolin Rosenbach,[4] Hung-Min Lin[5]
Naresh C. Osti,[6] Douglas L. Abernathy,[6] Wolfgang G. Zeier,[4,7] Olivier Delaire [1,5,8*]
[1] *Department of Mechanical Engineering and Materials Science, Duke University, Durham, NC 27708, USA*
[2] *John A. Paulson School of Engineering and Applied Sciences, Harvard University, Cambridge, MA 02138, USA*
[3] *Solid State Physics Division, Bhabha Atomic Research Centre Mumbai, Maharashtra 400085, India*
[4] *Institute of Inorganic and Analytical Chemistry, University of Münster, Münster D-48149, Germany*
[5] *Department of Chemistry, Duke University, Durham, North Carolina 27708, USA*
[6] *Neutron Scattering Division, Oak Ridge National Laboratory, Oak Ridge, Tennessee 37831, USA*
[7] *Institute of Energy Materials and Devices (IMD), IMD-4: Helmholtz-Institut Münster, Forschungszentrum Jülich, Münster 48149, Germany*
[8] *Department of Physics, Duke University, Durham, North Carolina 27708, USA*
[*] *To whom correspondence should be addressed; E-mail: olivier.delaire@duke.edu*

Superionic materials represent a regime intermediate between the crystalline and liquid states of matter. Despite the considerable interest in potential applications for solid-state batteries or thermoelectrics, it remains unclear whether the fast ionic diffusion observed in superionic materials reflects liquid-like dynamics or whether the hops of mobile ions are inherently coupled to more conventional lattice phonons. Here, we reveal a crossover from crystalline vibrations to relaxational dynamics of ionic diffusion in the superionic compound Li_6PS_5Cl, a candidate solid-state electrolyte. By combining inelastic and quasielastic neutron scattering measurements with first-principles based machine-learned molecular dynamics simulations, we find that the vibrational density of states in the superionic state strongly deviates from the quadratic behavior expected from the Debye law of lattice dynamics. The superionic dynamics emerge from overdamped phonon quasiparticles, giving rise to a linear density of states characteristic of instantaneous normal modes in the liquid state. Further, we show that the coupling of lattice phonons with a dynamic breathing of the Li^+ diffusion bottleneck enables an order-of-magnitude increase in diffusivity. Thus, our results shed new insights into superionics for future energy storage and conversion technologies.

Superionic conductors (SICs) are materials intermediate between the crystalline and liquid states of matter, and their unusual behavior has attracted fundamental interest for decades [1–3]. While retaining a partly crystalline character, SICs develop upon warming a sublattice of delocalized mobile ions with diffusivities comparable to those of liquids [1, 2]. They are attracting strong interest for their potential in applications such as solid-state batteries or thermoelectrics, yet their atomic structure and dynamics remain poorly understood. In crystals, harmonic phonons represent small-amplitude collective oscillations of atoms around an energy minimum at THz frequencies, propagating through the periodic lattice as quasiparticles, which successfully account for many thermodynamic and transport properties [4–6]. However, harmonic phonons are not *a priori* suited to describe complex dynamics in many condensed matter phases with strong disorder and large dynamical displacements, such as amorphous solids, liquids, or rotor phases and SICs.

Fundamentally different dynamics in these more complex phases are reflected in the violation of the Debye-law for the vibrational density of state (DOS) normally obeyed by crystalline solids: $g(\omega)\sim\omega^2$ at low frequency ω. In liquids, negative curvatures in the potential energy surface around intermittent local environments cause the phonon description to lead to a high density of modes with unphysical imaginary frequencies [7]. These so-called instantaneous normal modes (INMs) [8, 9] are manifested via anharmonic overdamped spectral responses that lead to a universal linear law for the DOS, $g(\omega)\sim\omega$ [10]. In amorphous solids, soft localized modes following another non-Debye scaling law [$g(\omega)\sim\omega^4$] are observed at low ω [11].

In SICs, the low-frequency behavior of $g(\omega)$ remains to be determined, an important point to assess their liquid-like vs solid-like nature. In addition, it is unclear to what extent the phonon-like dynamics expected for the crystalline framework couples with the hopping of ions on the mobile sublattice of the compound structure. To describe the hybrid dynamics of SICs in a unified approach, we adopt a conceptual framework beyond that of traditional quasiharmonic phonons, and consider the regime of overdamped spectra, guided by INMs in liquids.

While some observations of phonon quasiparticle breakdown have been reported in SICs [12–17], phonon modes derived from the parent crystalline lattice could still provide a convenient framework to glean insights into key diffusion steps around an ionic configuration, potentially serving as descriptors or enablers of fast diffusivity. Indeed, prior investigations of SICs and solid-state electrolytes established correlations of the enthalpy of migration (hopping barrier) with the low optical phonon frequencies or lower Debye and mean phonon frequencies

[18–21], and also correlated diffusion pre-factors with averaged lithium phonon frequencies [22, 23]. Vibrational and anharmonic characteristics were also recently considered as descriptors in a data-driven study [24].

From an applied perspective, the demand for rechargeable batteries with higher energy density, improved safety and reliability is driving the search for SICs with high lithium ion conductivity σ [25–28]. Sulfide solid-state electrolytes are among the most promising candidates thanks to high ionic conductivity comparable to liquid electrolytes, for instance $Li_{10}GeP_2S_{12}$ [29], $Li_{9.54}Si_{1.74}P_{1.44}S_{11.7}Cl_{0.3}$ [30], and argyrodite $Li_{5.5}PS_{4.5}Cl_{1.5}$ [31, 32] ($\sigma \sim$10−25 mS·cm^{-1}). The high σ of sulfide solid-state electrolytes has been associated with their soft lattice and highly polarizable S^{2-} anions, suggesting an underlying connection between fast diffusion and host lattice phonons [16, 20–22, 33–36], yet the role of phonons has remained difficult to ascertain owing to the highly complex structures and dynamics characteristic of solid-state electrolytes.

Here, we report important new insights by considering both strongly anharmonic phonon-derived vibrations of the crystalline lattice and stochastic hopping dynamics of the mobile Li^+ in Li_6PS_5Cl. To this end, we performed inelastic and quasielastic neutron scattering (INS and QENS), density functional theory and ab initio molecular dynamics (AIMD) simulations, augmented with machine-learning (MLMD), to reach nanosecond time-scales and to isolate key degrees-of-freedom. We uncover extreme damping and breakdown of soft anharmonic phonons associated with Li^+ motions, revealed in a low-energy spectral-weight enhancement. The signal follows the linear $g(\omega)\sim\omega$ characteristic of liquids and constitutes a signature of Li^+ hopping through extended anharmonic regions of the potential energy surface, disrupting long-range periodicity. It occurs concurrently with the enhanced QENS width that directly probes diffusivity, highlighting the intrinsic connection between low-energy vibrational and diffusive dynamics. We also establish the importance of phonons of the crystalline framework, showing how they enhance Li^+ diffusivity by an order of magnitude at ambient temperature. Vibrations of PS_4^{3-} are critical in opening up the structural bottleneck for long-range diffusion, while little effect of rotations ("paddle-wheel" mechanism) is observed. The picture emerging from our experiments and simulations bridges conventional diffusive and lattice vibrational models. Superseding simple quasiharmonic approximations and parametrizations in terms of averaged Li^+ vibrational frequencies [22, 23]. This picture extends pioneering connections between low energy phonon modes and ionic diffusion [18, 37] by integrating the concept of overdamped spectral functions associated with strongly anharmonic INMs [10, 38].

Spectral evolution from soft phonons to fast Li^+ diffusion

Non-Debye dynamics from superionic Li^+ diffusion:

We first reveal the emergence of non-Debye like behavior of $g(\omega)$ at low-ω in Li_6PS_5Cl upon warming. As shown in Fig. 1 (c), at 100 K, two phonon peaks are observed in the dynamical structure factor $S(E)$ ($E = \hbar\omega$) around 8 and 15 meV, but upon warming, the overall intensity increases with phonon occupations, and above 400 K, a clear quasielastic broadening develops around the elastic line, below $E < 4$ meV. This indicates a characteristic signal from fast intra-cage/doublet hops (the diffusion path is discussed later), and is reminiscent of spectral weight transfers observed in SICs with much heavier mobile cations (Ag^+, Cu^+ or Na^+) [12, 13, 16]. Strong softening and broadening for both peaks are observed, indicating phonon frequency renormalizations and enhanced phonon scattering rates as in a damped harmonic oscillator:

$$S(E) \propto (n + \frac{1}{2} \pm \frac{1}{2}) \frac{\Gamma E}{(E - E_0^2)^2 + (\Gamma E)^2} \qquad (1)$$

where Γ is the phonon linewidth and E_0 the undamped phonon frequency. The phonon DOS at 100 and 200 K extracted from INS exhibit a conventional Debye-like quadratic DOS at low frequency [$g(\omega) \sim \omega^2$], consistent with collective quasiharmonic dynamics of ions vibrating near the bottom of local potential minima [Fig. 1 (d,f)], see blue dashed line fit. However, at 600 K a qualitatively different regime emerges with a linear behavior (red dashed line). Note also that a small but finite spectral weight is expected to develop at $\omega = 0$. This represents diffusion, and will be discussed in more detail later. The linear and quadratic fits of $g(\omega)$ at other temperatures are summarized in Fig. S4 and Table. S1. For clarity, we emphasize that we are here referring to the Debye model of lattice dynamics, which describes collective atomic vibrations in a crystal with quantized normal modes (phonons) [40, 41]. This is distinct from the Debye equation describing the relaxation response of a dielectric medium in an external oscillating electric field [42–44].

The linear DOS $g(\omega) \sim \omega$ was recently derived from the Green's function as a universal response of liquids for a collection of INMs j [10]:

$$g(\omega) = \frac{1}{3\pi N} \sum_j \frac{\omega}{\omega^2 + \Gamma_j^2} \qquad (2)$$

where N is the total number of atoms, Γ_j is the relaxation rate of the jth INM, similar to the above phonon linewidth. A linear dependence results in the low frequency limit of overdamped INMs $\omega << \Gamma_j$:

$$g(\omega) = \alpha\omega + O(\omega^3),\ \alpha = \sum_j \frac{1}{3\pi N \Gamma_j^2} \qquad (3)$$

In addition to non-Debye behavior, the INS data in Fig. 1 (d) show a clear excess in spectral weight at low E. Figure 1 (e) shows a zoomed view of DOS curves without any vertical offset at 200 K and 600 K, obtained from INS (top panel) and MLMD (bottom panel). Extra intensity

is seen in spectrum at 600 K compared to 200 K (grey shaded area). Simulations reveal the predominant contribution of Li^+ dynamics in this excess spectral weight (dashed lines). Details in the temperature dependent spectra are discussed in Supplementary Information section 1.

A direct proportionality between the diffusion coefficient and the zero-energy limit of the spectral density, $g(\omega \to 0)$, can be derived from the velocity autocorrelation function $\langle v(0) \cdot v(t) \rangle$ (see Supplementary Information section 2 for derivations):

$$D = \frac{1}{3} \int_{-\infty}^{\infty} \langle v(0) \cdot v(t) \rangle dt \tag{4}$$

$$g(\omega) = \frac{1}{2\pi} \frac{\int_{-\infty}^{\infty} \langle v(0) \cdot v(t) \rangle e^{-i\omega t} dt}{\langle v(0) \cdot v(0) \rangle} \tag{5}$$

We estimate D=7.52×10^{-6} cm^2/s from MLMD $g(\omega \to 0)$ at 600 K, closely matching the values from both QENS and MLMD (see below). The corresponding values for $g(\omega \to 0)$ are 1.03±0.43 and 0.63±0.27 meV^{-1} for QENS and INS, respectively. Thus, both our experimental and computational probes of the low-E range of the THz spectrum (1 THz = 4.136 meV) let us identify the fast ionic hopping process. In fact, due to the fixed number of degrees-of-freedom, the breakdown of vibrational modes reflects the spectral weight transfer from local oscillation to diffusion.

Li^+ diffusion with QENS and MLMD

Crystal structure and diffusion path: Next, we investigate the Li^+ diffusion path and associated time-scales through combined QENS, INS and simulations. Lithium argyrodites have the general composition Li_7PnCh_6, where Pn = P or As and Ch = O, S, Se can be replaced with halogens (X), as in Li_6PS_5X (X = Cl, Br, I) [32]. Fig. 1 (a) shows the unit cell of Li_6PS_5X (space group $F\bar{4}3m$). At low-T, Li^+ mainly occupy Wyckoff 48h sites (T5) surrounding the 4c S^{2-}, and partly 24g (T5a) and type 2 (T2) with overall 50% occupancy, as shown from our MLMD computation of Li^+ probability (Fig. **??**). This is in agreement with neutron diffraction measurements [45]. Arrows in Fig. 1 represent the three hopping processes defined in Refs. 16, 46. The actual hops occur through intermediate sites, namely: (i) doublet hops (T5-T5a-T5); (ii) intra-cage hops (T5-T2-T5); and (iii) inter-cage hops (T5-T2-T2-T5) [20, 45, 48]. The inter-cage hopping rate is an order-of-magnitude lower than the other rates, and is thus the bottleneck for long-range diffusion. These processes are confirmed by the computed Li^+ probability distribution from MLMD at 600 K [Fig. 1 (b)]. A proposed T1x site [49] is not observed in our simulations, however (detailed in Supplementary Information section 3). Below, we will clarify the atomistic mechanisms enabling fast Li^+ diffusion, and isolate key host vibrational modes.

Resolving multiple hopping timescales: We determine the diffusion coefficient from QENS data, shown in Fig. 2 (a). The central peak broadening beyond the intrinsic instrument resolution [Fig. S7] is a Lorentzian signature of ionic diffusion [50], see *e.g.,* 400 K *vs* 300 K. Based on our MLMD simulations [Fig. S11], the slow signal below 0.1 meV corresponds to the bottleneck inter-cluster hops, and the faster intra-cluster hops contribute to the linear DOS region observed in INS. A typical fit of QENS data (T = 600 K, Q = 1.5±0.1 Å^{-1}) is shown in Fig. 2 (b), consisting of three terms: elastic intensity (delta function), QENS (Lorentzian), and a linear background. The Lorentzian half-width at half-maximum (HWHM) increases with momentum transfer Q and plateaus around 1.5 Å^{-1}. This behavior is expected for jump diffusion on a lattice and is captured well by a Chudley-Elliot model, as shown in Fig. 2 (c). From this, we can extract a diffusion coefficient D, jump length d and residence time τ (see Methods). At 600 K, the estimated inter-cage hopping coefficient is D=(5.0±2.1)×10^{-6} cm^2/s, in good agreement with reported MD simulations of long-range diffusion. A detailed summary of diffusion coefficients and activation energies from previous references is provided in Supplementary Information section 4. At 300 K, D=(0.7±0.2)×10^{-6} cm^2/s lies in the range of the reported values from impedance measurements (10^{-9} to 10^{-5} cm^2/s). D increases and τ decreases with increasing temperature (Fig. S8), and an activation energy of 0.11 eV can be estimated from the Arrhenius fit of D *vs* T. This value is smaller than estimates from nuclear magnetic resonance for long-range diffusion, which lie in the range of 0.132 to 0.35 eV, or the values of 0.16 to 0.45 eV from electrochemical impedance spectroscopy. While both QENS and nuclear magnetic resonance probe microscopic ionic conduction, a higher E_a value in nuclear magnetic resonance measurements is a common observation across various systems. The larger values inferred from impedance measurements could originate from boundary and contact resistances, or voids in samples.

To resolve the distinct timescales between the slow inter-cage hops and the ten-times faster intra-cage/doublet hops, we directly simulate the neutron spectra with MLMD trajectories over 1 ns (3.2 μeV energy resolution), and approaching the experimental resolution of 3.5 μeV at BASIS. Importantly, the simulated spectra consist of two Lorentzians, one below 0.1 meV and one around 1 meV (Fig. S10). The narrower component reflecting less-frequent inter-cage hops is in excellent agreement with QENS [Fig. 2 (b)]. The corresponding diffusion coefficients from QENS and MLMD are 5.0×10^{-6} and 6.6×10^{-6} cm^2/s, respectively and the jump lengths (d_{jump} = 2.4±0.4 Å and 2.7±0.1 Å) match the crystallographic inter-cage hopping distance. The wider spectral component, corresponding to the fast intra-cage/doublet hops, has a ten-times larger width and thus ten-times shorter τ (Table. I). The estimate for fast processes is an average of intra-cage

and doublet hops, thus leading to a larger uncertainty in the corresponding D, and the estimated d_{jump} = 1.2±0.1 Å is the average of the T5-T5a (0.8 Å) and T5-T2 distances (1.5 Å) [Fig. 1 (b)]. Moreover, the HWHM from QENS measurement at large $|\mathbf{Q}|$ (e.g., $|\mathbf{Q}|$=1.5 Å) is 87.4±2.7 μeV at 600K. If this QENS signal resulted from fast intra-cage hopping, then an order-of-magnitude narrower component from a slower process would be expected, and could still be resolved (the BASIS resolution is 3.5 μeV), but such a slow component is not observed. Hence, this QENS broadening must be contributed by inter-cage hopping. This is also consistent with the MLMD estimated QENS width from inter-cage hopping. Further, the diffusion coefficient is also estimated from the computed window-averaged mean square displacements (MSD) *vs* time via the Einstein formula (trajectory lengths over 500 ps, Fig. S7). Our MSD calculations quantitatively agree with the AIMD simulation at 500 K in Ref. 16. An Arrhenius fit provides an activation barrier of 0.16 eV, close to the value of 0.11 eV from QENS, also in good agreement with the values of 0.18 eV from AIMD in Ref. 51. Thus, combining QENS experiments and simulations, we fully resolved the spatial and temporal characteristics of the complex diffusion process in Li_6PS_5Cl, benchmarking our MLMD approach. Finally, we further analyzed the diffusive dynamics by tallying all inter-cage hops in the MLMD trajectories (detailed in Supplementary Information section 5). Spherical cage boundaries were defined with respect to a central S or Cl ion at Wyckoff 4*c* sites [Fig. S16 (b)] and used to identify Li^+ inter-cage jumps. Accounting for all jumps in 19 parallel nanosecond-long MLMD simulations at 600K, we obtained average Li^+ inter-cage hopping timescales (mean cage residence time) of 24, 37, and 51 ps for cage radii of 4.0, 3.75, 3.5 Å, respectively. These results are in good agreement with the residence time from our Chudley-Elliot fits in Table. I. Our estimate of hopping timescale agrees well with the AIMD results of Klerk et al [46]. Deviations may originate from the larger unit cell and longer simulation used in our MLMD, which provides better statistics. It is expected that smaller spherical cages miss some inter-cage jumps as they do not account for the whole region connecting cages..

Facile Li^+ diffusion from anharmonic phonons

Evolution from vibrational to diffusive dynamics: Examining the neutron-weighted spectra from MLMD in Fig. S3, we see that the Li spectral weight originally at high energy (>25 meV) shifts toward lower frequencies on warming, while only a slight broadening occurs for S, P, and Cl spectra. Surprisingly, as the diffusion coefficients increased by 300× from 200 K to 600 K (0.0522×10^{-6} to 15.9×10^{-6} cm^2/s), the averaged Li band center only softened by −5% (33.56 to 32.04 meV). However, the low-E (<10 meV) Li spectral intensity is much more sensitive, and increases by 60%. Furthermore, comparing vibrational spectra from MLMD with various constraints [Fig. 3 (c) and S6], we find that the suppression of high energy modes is not critical for fast ionic diffusion. The humps at 30, 50, and 60 meV are associated with internal motions of the PS_4^{3-} unit, which vanish for rigid PS_4^{3-}, while the rotational modes of PS_4^{3-} contribute strongly at 20 meV. High energy modes involving Li^+ motions show some variation around 50 meV, which may be related to the vibrations of S in PS_4^{3-}. A recent study suggested that low-E polyanion rotational modes couple with these high-E Li modes and are less important for Li^+ diffusion [52]. The largest effect occurs below 10 meV, and the value of $g(\omega \to 0)$ is finite in all the cases featuring fast diffusion, following the estimated diffusion coefficients from MSD. Strikingly, in the case of fixed PS_4^{3-} and fixed host, the spectral weight below 10 meV is strongly suppressed [Fig. 3 (c)], which concurs with the abrupt decrease in the diffusion coefficient.

Dynamic breathing of the structural bottleneck: We now probe the correlation of Li^+ diffusion with the flexibility of the argyrodite structure. In Fig. 3 (a,b), we compare trajectories of a specific Li^+ over 500 ps, computed from MLMD without constraints or with fixed host, respectively. The unconstrained trajectory shows long-range Li^+ diffusion spanning multiple different cages and containing more than ten inter-cage jumps (see also Fig. **??**). Interestingly, the Li^+ ion in Fig. 3 (a) explores each cage (green segments) for a relatively long time, yet inter-cage hops occur very fast, within 0.5 ps (red segments). In contrast, inter-cage hops are strongly suppressed when the host framework is fixed [Fig. 3 (b)]. Therefore, the host lattice vibrations play a crucial role in enabling long-range diffusion. Additional examples of trajectories for both cases are shown in Fig. S14, S15. To gain a finer understanding of this process, in Fig. 3 (c) inset, we zoom in on the structural bottleneck between adjacent T5-T2 and T2-T2 sites (see also Fig. S22, S23 and Supplementary Information section 6). The time-averaged bottleneck area exhibits a wider distribution when unconstrained. This shows the importance of dynamic breathing of the structural bottleneck for Li^+ diffusion. The trends in dynamic breathing also highlight the anharmonic nature of the potential. The interatomic potential energy surface is anharmonic and shallow, "frustrated" in the sense that there is not a single deep locally-harmonic minimum in the configurational space. The thermal energy at 600 K already allows Li^+ to explore wide swaths of this shallow surface along its diffusion path.

Overdamped vibrational regime: We further investigate the spectral functions of specific phonon modes and evaluate their broadening in the superionic regime. From MLMD trajectories, we calculated the momentum-resolved dynamical susceptibility, $\chi''(\mathbf{Q},\omega)$, shown in Fig. 3 (d-f) (see Supplementary Information section 7). We find that the longitudinal-polarized phonons are

already very broad (anharmonic) at 50 K but broaden even more at 600 K. The transverse-polarized phonons near the zone boundary, where a dominant contribution from Li^+ is expected, completely break down into an overdamped response [Fig. 3 (f)]. This behavior is consistent with overdamped INM behavior and is reminiscent of observations in Ag^+ [13] or Na^+ conductors [53].

Identifying key host vibrations: To resolve the host vibrations that most strongly affect Li^+ diffusion, we implemented five different constraints in MLMD: (i) making PS_4^{3-} units rigid bodies (green diamonds) that can rotate or translate as a whole; (ii) rigid PS_4^{3-} units with frozen rotations (brown triangles), only allowing translational vibrations ("wiggling"); (iii) fixing S and P ions in PS_4^{3-} units to their initial positions (blue pentagons), while free S, Cl and Li ions are mobile; (iv) fixing positions of all free S and Cl ions (pink hexagons); (v) fixing all framework ions (P, S, Cl), with only Li^+ mobile (black crosses). As shown in Fig. 2 (d), we clearly see that making PS_4^{3-} units rigid (constraint i) minimally impacts D. Further, comparing cases (ii) (wiggling-only) *vs* (iii) (fixed PS_4^{3-}) shows that wiggling of PS_4^{3-} is more conducive to Li^+ diffusion (see brown *vs* blue markers). This agrees with a MD investigation of $Na_{3-x}Sb_{1-x}W_xS_4$ [54]. Recently, polyhedral anion rotations and re-orientations in so-called "rotor" or "plastic" phases have attract particularly strong interest in solid-state electrolytes [55–57]. However, full re-orientations of PS_4^{3-} are not observed in our MLMD at 600 K (Fig. S20). We find rotations of limited amplitudes, similar to prior results in a Cu-based argyrodite [16]. Our observations are consistent with a recent report that attributes fast diffusion to an occupancy-change-driven tilting (soft-cradle effect), rather than a paddle wheel effect [58]. The angular autocorrelation function averaged over all P-S pairs was further analyzed at 300 and 600 K [Fig. S20 (d) and Supplementary Information section 8], which shows the lack of PS_4^{3-} reorientations (self-correlated P-S bond direction). The small decrease at 600 K is ascribed to larger-amplitude atomic vibrations.

When all framework ions are immobilized, the rigid bottleneck strongly constrains Li^+ diffusion [Fig. 2 (d)]. This is further corroborated through an analysis of fluctuations of the bottleneck cross-sectional areas, shown in Fig. S22. Unlocking host dynamics enables wider-amplitude fluctuations and facilitates inter-cage diffusion. Importantly, our results show that the host vibrations modulate the diffusion coefficient by $\sim 10\times$ at room temperature, even in a soft polarizable material already including compositional disorder. We note that such effects could be missed if performing only high-T MD simulations. At 600 K, the enhancement is more modest ($\sim 3\times$) because the thermal energy already allows Li^+ to explore wider regions of the interatomic potential energy surface.

CONCLUSION AND OUTLOOK

In summary, we integrated neutron scattering and machine-learning augmented first-principles simulations to gain new insights into the complex atomic dynamics of the solid-state electrolyte Li_6PS_5Cl, revealing a crossover from phonon quasiparticles typical of crystals toward the relaxational behavior and intrinsic normal modes characteristic of liquids. These insights into the microscopic mechanism of fast Li^+ diffusion in argyrodites could guide the design of future materials for solid-state electrolytes. In the superionic regime, Li^+ ions undergo fast stochastic hopping across a shallow potential energy landscape, which is facilitated by the dynamics of the crystalline framework. Specific phonon modes of the soft crystalline lattice enable an order-of-magnitude enhancement in Li^+ ion diffusivity at ambient temperature, through the dynamic breathing of hopping bottlenecks. Therefore, this suggests tailoring the dynamics of the host framework to optimize ionic conductivity of solid-state electrolytes.

ACKNOWLEDGEMENTS

Neutron scattering data collection, MD simulations and analysis by JD, simulations by H-ML, as well as manuscript writing (JD, OD), were supported by a U.S. National Science Foundation DMREF project under award DMR-2119273. Initial analysis and simulations by MKG were supported by DOE award DE-SC0019978. Sample synthesis by CR and WGZ was supported by the Deutsche Forschungsgemeinschaft under grant number ZE 1010/4-1. The use of Oak Ridge National Laboratory's Spallation Neutron Source was sponsored by the Scientific User Facilities Division, Office of Basic Energy Sciences, U.S. DOE. Theoretical calculations were performed using the National Energy Research Scientific Computing Center, a U.S. DOE Office of Science User Facility supported by the Office of Science of the U.S. DOE under Contract No. DE-AC02-05CH11231.

AUTHOR CONTRIBUTIONS

OD and JD designed the research. JD, MKG, NCO, and DLA performed neutron scattering measurements. CR and WGZ synthesized and characterized the samples. JD, MKG, and H-ML performed simulations and analyzed data. JD and OD wrote the paper.

COMPETING INTERESTS

The authors declare no competing interests.

TABLES

	BASIS	MLMD narrow	MLMD wide
d_{jump} (Å)	2.4±0.4	2.7±0.1	1.2±0.1
τ (ps)	19.2±2.4	18.6±0.6	1.2±0.2
D (x10^{-6} cm^2/s)	5.0±2.1	6.6±0.7	20.5±8.2

TABLE I. Hopping distances, residence time and diffusion coefficients at 600 K of QENS spectra from BASIS and MLMD, both from Chudley-Elliot analysis. MLMD narrow and wide represents slow inter-cage and fast intra-cage/doublet processes, respectively.

FIGURE LEGENDS/CAPTIONS

FIG. 1. (color) **Quadratic to linear vibrational spectrum reveals non-Debye dynamics in solid electrolyte.** (a) Crystal structure of Li_6PS_5Cl. Li, P, S, and Cl atoms are shown in green-white, purple, yellow, and brown, respectively. Cl^- form a face-centered cubic lattice (Wyckoff 4*a*) with PS_4^{3-} units in the octahedral sites centered at P^{5+} (Wyckoff 4*b*), and surrounded by S^{2-} in the Wyckoff 16*e* sites. The remaining S^{2-} ("free S") occupy half of the tetrahedral sites (Wyckoff 4*c*). Li^+ occupy the Wyckoff 48*h* sites surrounding the 4*c* S^{2-} with 50% occupancy. (b) Probability distribution of Li^+ at 600 K with isosurfaces value 2×10^{-11} Bohr^{-3} computed from MLMD. Arrows in (a) show three conventional types of Li^+ hops reported in the literature, Li^+ probability in (b) shows that diffusion occurs through intermediate sites (see text). (c) $S(E)$ at $E_i = 25$ measured at ARCS at 100, 200, 300, 400, 500, 600, and 680 K. (d) Corresponding vibrational spectra. The dashed lines are the replica of the 100 K data with the same offset as references. The shoulder around 8 meV and the peak at 15 meV broaden with increasing temperature as a result of the enhanced phonon-phonon scattering. Strong softening is observed. (e) Low-E spectrum from INS (top) and MLMD (bottom). A finite spectral weight at $\omega \to 0$ is observed in both INS and MLMD at 600 K from Li^+ diffusion. The $g(\omega \to 0)$ estimated from the hopping coefficient in QENS is plotted as purple cross. Shaded regions represent the difference between the two INS spectra or the calculated Li partial DOS from MLMD. (f) Linear and quadratic fit of low-E INS spectrum. At 200 K, spectral intensity increases quadratically with energy. At 600 K, clear excess spectral intensity (no vertical offset) and linear frequency dependence are observed, strongly deviating from Debye model. The INS data below 1.5 meV are removed (elastic scattering from ARCS resolution). The error bars represent one standard deviation which include statistical uncertainties of the neutron flux.

FIG. 2. (color) **Ionic diffusion from back-scattering spectroscopy and MLMD.** (a) Temperature dependent QENS spectra of $^7Li_6PS_5Cl$, measured at $Q = 1.5\pm0.1$ Å^{-1} at 100, 300, 400, 500, 600, and 680 K, offset vertically. Upon heating above 300 K, clear broadening is observed, as a characteristic of decaying correlation from ionic diffusion. Factors of 2, 3 and 4 are applied for 500, 600, and 680 K, respectively, to help visualizing the broadening. (b) The QENS fit at 600 K, with raw data (grey), and the total fit (orange). QENS spectra are fitted with a delta function (blue), a lorentzian (red), and a linear background (black), convoluted with the instrument resolution (30 K measurements). MLMD calculated spectrum for slow inter-cage diffusion is shown in green. (c) Chudley-Elliot fits at 600 K from BASIS (blue) and MLMD (orange). Γ is the HWHM. (d) Arrhenius plot of the diffusion coefficients. An activation energy of 0.11 and 0.16 eV are estimated from QENS and MLMD, respectively. The error bars represent one standard deviation which include statistical uncertainties of the neutron flux.

FIG. 3. (color) **Effect of lattice flexibility on ionic diffusion and selective breakdown of phonon quasiparticles.** (a) Selected sub-trajectory (500 ps) at 600 K for unconstrained MLMD showing a Li^+ exploring multiple cages. The green trajectory is that of a single Li^+ ion across multiple cages. (b) Li^+ trajectory (500 ps) at 600 K for fixed host case. Long-range diffusion is inhibited by the rigid structural bottleneck. Red segments highlight 0.2 ps portions of the trajectories corresponding to inter-cage hops. Back-and-forth jumps within 1 ps are removed. Black box indicates the unit-cell. (c) Li PDOS for several MLMD constraints. Higher intensity and zero-limit value is observed for unconstrained case (higher diffusion coefficient) in contrast with the fixed PS_4^{3-} and fixed host cases. Inset shows the time-averaged area distributions of the structrual bottleneck between adjacent T2-T2 sites. (d) MLMD calculated $\chi''(\mathbf{Q},\omega)$ for longitudinal modes along [0,0,L] at 600 K. 1D spectral functions for (e) longitudinal acoustic phonons at $\mathbf{Q}$=0,0,0.5 (r.l.u.) and (f) Transverse acoustic phonons at $\mathbf{Q}$=0,1.5,4 (r.l.u.). At 600 K, longitudinal acoustic phonons become very broad and the breakdown of short wavelength transverse acoustic phonons is observed due to the disruption of long-range periodicity from the diffusion Li^+.

REFERENCES

[1] Gerald D Mahan and Walter L Roth, editors. Superionic Conductors. Springer US, Boston, MA, 1976.

[2] J. B. Boyce and B. A. Huberman. Superionic conductors: Transitions, structures, dynamics. Physics Reports, 51:189–265, 1979.

[3] M. Parrinello, A. Rahman, and P. Vashishta. Structural transitions in superionic conductors. Phys. Rev. Lett., 50:1073–1076, Apr 1983.

[4] Paul M Chaikin, Tom C Lubensky, and Thomas A Witten. Principles of condensed matter physics, volume 10. Cambridge university press Cambridge, 1995.

[5] Göran Grimvall. Thermophysical properties of materials. Elsevier, 1999.

[6] Peter Brüesch. Phonons: Theory and experiments I: Lattice dynamics and Models of interatomic forces, volume 34. Springer Science & Business Media, 2012.

[7] Norman Henry March and Mario P Tosi. Atomic dynamics in liquids. Courier Corporation, 1991.

[8] Richard M Stratt. The instantaneous normal modes of liquids. Accounts of Chemical Research, 28(5):201–207, 1995.

[9] T Keyes. Instantaneous normal mode approach to liquid state dynamics. The Journal of Physical Chemistry A, 101(16):2921–2930, 1997.

[10] Alessio Zaccone and Matteo Baggioli. Universal law for the vibrational density of states of liquids. Proceedings of the National Academy of Sciences, 118(5):e2022303118, 2021.

[11] Hideyuki Mizuno, Hayato Shiba, and Atsushi Ikeda. Continuum limit of the vibrational properties of amorphous solids. Proceedings of the National Academy of Sciences, 114(46):E9767–E9774, 2017.

[12] Jennifer L Niedziela, Dipanshu Bansal, Andrew F May, Jingxuan Ding, Tyson Lanigan-Atkins, Georg Ehlers, Douglas L Abernathy, Ayman Said, and Olivier Delaire. Selective breakdown of phonon quasiparticles across superionic transition in $CuCrSe_2$. Nature Physics, 15(1):73, 2019.

[13] Jingxuan Ding, Jennifer L Niedziela, Dipanshu Bansal, Jiuling Wang, Xing He, Andrew F May, Georg Ehlers, Douglas L Abernathy, Ayman Said, Ahmet Alatas, et al. Anharmonic lattice dynamics and superionic transition in agcrse2. Proceedings of the National Academy of Sciences, 117(8):3930–3937, 2020.

[14] L Xie, JH Feng, R Li, and JQ He. First-principles study of anharmonic lattice dynamics in low thermal conductivity agcrse 2: Evidence for a large resonant four-phonon scattering. Physical Review Letters, 125(24):245901, 2020.

[15] Chen Wang and Yue Chen. Highly selective phonon diffusive scattering in superionic layered $AgCrSe_2$. npj Computational Materials, 6(1):1–6, 2020.

[16] Mayanak K Gupta, Jingxuan Ding, Dipanshu Bansal, Douglas L Abernathy, Georg Ehlers, Naresh C Osti, Wolfgang G Zeier, and Olivier Delaire. Strongly anharmonic phonons and their role in superionic diffusion and ultralow thermal conductivity of cu7pse6. Advanced Energy Materials, page 2200596, 2022.

[17] Gabriel Krenzer, Chang-Eun Kim, Kasper Tolborg, Benjamin J Morgan, and Aron Walsh. Anharmonic lattice dynamics of superionic lithium nitride. Journal of Materials Chemistry A, 10(5):2295–2304, 2022.

[18] Kunio Wakamura. Roles of phonon amplitude and low-energy optical phonons on superionic conduction. Physical Review B, 56(18):11593, 1997.

[19] Matthias T Agne, Joop Frerichs, Shuo Wang, Georg Dewald, Tim Bernges, Nella Vargas-Barbosa, Yifei Mo, Michael Hansen, and Wolfgang Zeier. Relating critical phonon occupation to activation barrier in fast lithium-ion conductors. 2022.

[20] Marvin A Kraft, Sean P Culver, Mario Calderon, Felix Böcher, Thorben Krafuskopf, Anatoliy Senyshyn, Christian Dietrich, Alexandra Zevalkink, Jürgen Janek, and Wolfgang G Zeier. Influence of lattice polarizability on the ionic conductivity in the lithium superionic argyrodites li6ps5x (x= cl, br, i). Journal of the American Chemical Society, 139(31):10909–10918, 2017.

[21] Thorben Krauskopf, Sokseiha Muy, Sean P Culver, Saneyuki Ohno, Olivier Delaire, Yang Shao-Horn, and Wolfgang G Zeier. Comparing the descriptors for investigating the influence of lattice dynamics on ionic transport using the superionic conductor na3ps4–xsex. Journal of the American Chemical Society, 140(43):14464–14473, 2018.

[22] Sokseiha Muy, John C Bachman, Livia Giordano, Hao-Hsun Chang, Douglas L Abernathy, Dipanshu Bansal, Olivier Delaire, Satoshi Hori, Ryoji Kanno, Filippo Maglia, et al. Tuning mobility and stability of lithium ion conductors based on lattice dynamics. Energy and Environmental Science, 11(4):850–859, 2018.

[23] Sokseiha Muy, Johannes Voss, Roman Schlem, Raimund Koerver, Stefan J Sedlmaier, Filippo Maglia, Peter Lamp, Wolfgang G Zeier, and Yang Shao-Horn. High-throughput screening of solid-state li-ion conductors using lattice-dynamics descriptors. Iscience, 16:270–282, 2019.

[24] Cibrán López, Agustí Emperador, Edgardo Saucedo, Riccardo Rurali, and Claudio Cazorla. Universal ion-transport descriptors and classes of inorganic solid-state electrolytes. Materials horizons, 10(5):1757–1768, 2023.

[25] Dominique Larcher and Jean-Marie Tarascon. Towards greener and more sustainable batteries for electrical energy storage. Nature chemistry, 7(1):19–29, 2015.

[26] John B Goodenough and Kyu-Sung Park. The li-ion rechargeable battery: a perspective. Journal of the American Chemical Society, 135(4):1167–1176, 2013.

[27] Jürgen Janek and Wolfgang G Zeier. A solid future for battery development. Nature Energy, 1(9):1–4, 2016.

[28] Theodosios Famprikis, Pieremanuele Canepa, James A Dawson, M Saiful Islam, and Christian Masquelier. Fundamentals of inorganic solid-state electrolytes for batteries. Nature materials, 18(12):1278–1291, 2019.

[29] Noriaki Kamaya, Kenji Homma, Yuichiro Yamakawa, Masaaki Hirayama, Ryoji Kanno, Masao Yonemura, Takashi Kamiyama, Yuki Kato, Shigenori Hama, Koji Kawamoto, et al. A lithium superionic conductor. Nature materials, 10(9):682, 2011.

[30] Yuki Kato, Satoshi Hori, Toshiya Saito, Kota Suzuki, Masaaki Hirayama, Akio Mitsui, Masao Yonemura, Hideki Iba, and Ryoji Kanno. High-power all-solid-state batteries using sulfide superionic conductors. Nature Energy, 1(4):1–7, 2016.

[31] Parvin Adeli, J David Bazak, Kern Ho Park, Ivan Kochetkov, Ashfia Huq, Gillian R Goward, and Linda F Nazar. Boosting solid-state diffusivity and conductivity in lithium superionic argyrodites by halide substitution. Angewandte Chemie, 131(26):8773–8778, 2019.

[32] Hans-Jörg Deiseroth, Shiao-Tong Kong, Hellmut Eckert, Julia Vannahme, Christof Reiner, Torsten Zaiß, and Marc Schlosser. Li6ps5x: a class of crystalline li-rich solids with an unusually high li+ mobility. Angewandte Chemie International Edition, 47(4):755–758, 2008.

[33] P Brüesch, L Pietronero, S Strässler, and HR Zeller. Brownian motion in a polarizable lattice: Application to superionic conductors. Physical Review B, 15(10):4631, 1977.

[34] Qing Zhang, Daxian Cao, Yi Ma, Avi Natan, Peter Aurora, and Hongli Zhu. Sulfide-based solid-state electrolytes: synthesis, stability, and potential for all-solid-state batteries. Advanced Materials, 31(44):1901131, 2019.

[35] Roman Schlem, Michael Ghidiu, Sean P Culver, Anna-Lena Hansen, and Wolfgang G Zeier. Changing the static and dynamic lattice effects for the improvement of the ionic transport properties within the argyrodite li6ps5–x se x i. ACS Applied Energy Materials, 3(1):9–18, 2019.

[36] I Hanghofer, M Brinek, SL Eisbacher, B Bitschnau, M Volck, V Hennige, I Hanzu, D Rettenwander, and HMR Wilkening. Substitutional disorder: structure and ion dynamics of the argyrodites li6ps5cl, li6ps5br and li6ps5i. Physical Chemistry Chemical Physics, 21(16):8489–8507, 2019.

[37] Ulrich Köhler and Christian Herzig. On the correlation between self-diffusion and the low-frequency la –<111> phonon mode in bcc metals. Philosophical Magazine A, 58(5):769–786, 1988.

[38] Caleb Stamper, David Cortie, Zengji Yue, Xiaolin Wang, and Dehong Yu. Experimental confirmation of the universal law for the vibrational density of states of liquids. The Journal of Physical Chemistry Letters, 13(13):3105–3111, 2022.

[39] Mayanak K Gupta, Jingxuan Ding, Naresh C Osti, Douglas L Abernathy, William Arnold, Hui Wang, Zachary Hood, and Olivier Delaire. Fast na diffusion and anharmonic phonon dynamics in superionic na 3 ps 4. Energy & Environmental Science, 14(12):6554–6563, 2021.

[40] Martin T Dove. Introduction to lattice dynamics. Number 4. Cambridge university press, 1993.

[41] Peter Brüesch. Phonons: Theory and Experiments I, volume 34 of Springer Series in Solid-State Sciences. Springer Berlin Heidelberg, Berlin, Heidelberg, 1982.

[42] K Funke. Jump relaxation in solid electrolytes. Progress in Solid State Chemistry, 22(2):111–195, 1993.

[43] Andrew K Jonscher. Dielectric relaxation in solids. Journal of Physics D: Applied Physics, 32(14):R57, 1999.

[44] Junko Habasaki, Carlos Leon, and KL Ngai. Dynamics of glassy, crystalline and liquid ionic conductors. Top Appl Phys, 132:355–410, 2017.

[45] Nicolo Minafra, Marvin A Kraft, Tim Bernges, Cheng Li, Roman Schlem, Benjamin J Morgan, and Wolfgang G Zeier. Local charge inhomogeneity and lithium distribution in the superionic argyrodites li6ps5x (x= cl, br, i). Inorganic Chemistry, 59(15):11009–11019, 2020.

[46] Niek JJ De Klerk, Irek Rosło, and Marnix Wagemaker. Diffusion mechanism of li argyrodite solid electrolytes for li-ion batteries and prediction of optimized halogen doping: the effect of li vacancies, halogens, and halogen disorder. Chemistry of Materials, 28(21):7955–7963, 2016.

[47] Benjamin J Morgan. Mechanistic origin of superionic lithium diffusion in anion-disordered li6ps5 x argyrodites. Chemistry of Materials, 33(6):2004–2018, 2021.

[48] Shiao-Tong Kong, Hans-Jörg Deiseroth, Christof Reiner, Özgül Gün, Elmar Neumann, Clemens Ritter, and Dirk Zahn. Lithium argyrodites with phosphorus and arsenic: order and disorder of lithium atoms, crystal chemistry, and phase transitions. Chemistry–A European Journal, 16(7):2198–2206, 2010.

[49] Enyue Zhao, Lunhua He, Zhigang Zhang, Jean-Marie Doux, Darren HS Tan, Erik A Wu, Grayson Deysher, Yu-Ting Chen, Jinkui Zhao, Fangwei Wang, et al. New insights into li distribution in the superionic argyrodite li 6 ps 5 cl. Chemical Communications, 57(82):10787–10790, 2021.

[50] Tasso Springer. Quasielastic neutron scattering for the investigation of diffusive motions in solids and liquids. Springer Tracts in Modern Physics, Volume 64, pages 1–100, 1972.

[51] Xuyong Feng, Po-Hsiu Chien, Yan Wang, Sawankumar Patel, Pengbo Wang, Haoyu Liu, Marcello Immediato-Scuotto, and Yan-Yan Hu. Enhanced ion conduction by enforcing structural disorder in li-deficient argyrodites li6- xps5- xcl1+ x. Energy Storage Materials, 30:67–73, 2020.

[52] Zhenming Xu, Xi Chen, Hong Zhu, and Xin Li. Anharmonic cation-anion coupling dynamics assisted lithium-ion diffusion in sulfide solid electrolytes. Advanced Materials, page 2207411, 2022.

[53] Mayanak Kumar Gupta, Sajan Kumar, Ranjan Mittal, and Samrath L Chaplot. Soft-phonon anharmonicity, floppy modes, and na diffusion in na 3 f y (y= s, se, te): Ab initio and machine-learned molecular dynamics simulations. Physical Review B, 106(1):014311, 2022.

[54] Jeffrey G Smith and Donald J Siegel. Ion migration mechanisms in the sodium sulfide solid electrolyte na3–x sb1–x w x s4. Chemistry of Materials, 34(9):4166–4171, 2022.

[55] Douglas R MacFarlane and Maria Forsyth. Plastic crystal electrolyte materials: new perspectives on solid state ionics. Advanced materials, 13(12-13):957–966, 2001.

[56] Zhizhen Zhang and Linda F Nazar. Exploiting the paddle-wheel mechanism for the design of fast ion conductors. Nature Reviews Materials, pages 1–17, 2022.

[57] Hong Fang and Puru Jena. Argyrodite-type advanced lithium conductors and transport mechanisms beyond peddle-wheel effect. Nature communications, 13(1):1–11, 2022.

[58] KyuJung Jun, Byungju Lee, Ronald L. Kam, and Gerbrand Ceder. The nonexistence of a paddlewheel effect in superionic conductors. Proceedings of the National Academy of Sciences, 121(18):e2316493121, 2024.

METHODS

Sample Preparation: We synthesis $^{7}Li_6PS_5Cl$ to minimize the strong neutron absorption of ^{6}Li. Stoichiometric amounts of $^{7}LiCl$ (99 atom% ^{7}Li, Sigma-Aldrich), $^{7}Li_2S$ ($\geq$99 atom% ^{7}Li, Sigma-Aldrich) and P_2S_5 (Sigma-Aldrich) were hand ground in an agate mortar for 15 minutes. The ground powder was pressed into pellets and sealed into carbon coated quartz ampoules, the quartz ampoules were preheated under dynamic vacuum at 800 °C for 2 hours. The solid-state reaction took place in a Nabertherm furnace for 2 weeks at 550 °C with a heating ramp of 100 °C/h and cooled naturally. The obtained product was hand ground and sealed under vacuum (4.2×10^{-1} mbar) in a 10 mm quartz ampoule for the measurement of the neutron diffraction data. Diffraction patterns from a StadiP X-Ray diffractometer from STOE in Debye-Scherrer geometry with a

Cu-Kα radiation (λ1=1.545 Å) were compared with the theoretical diffraction pattern generated using the CrystalDiffract diffraction software (CrystalMaker Software Ltd, Oxford, England, www.crystalmaker.com). The relative intensity and peak positions are in very good agreement.

Quasielastic Neutron Scattering: The QENS measurements were performed using the BASIS backscattering spectrometer at the Spallation Neutron Source, Oak Ridge National Laboratory [1]. 6 grams of $^7Li_6PS_5Cl$ were flame sealed in two fused-silica ampoules. The ampoules were aligned and wrapped together with aluminum foil to approximate a flat plate geometry. Another two empty ampoules with identical configurations are used to collect empty can signal. Si(111) analyzers was used with neutron wavelength 6.4 Å and chopper frequency of 60 Hz. This configuration yields an energy bandwidth of $-100 < E < 100\,\mu$eV with energy resolution 3.5 μeV, and a momentum transfer coverage of $0.2 < Q < 2.0\,\text{Å}^{-1}$. Samples are mounted in a thin wall aluminum can in a top-loading closed-cycle refrigerator. We measured $T = 30$, 100, 200, 300, 400, 450, 500, 550, 600, and 680 K. The 30 K data shows no broadening, which is used as a sample dependent resolution function. The collected data from the area detectors were transformed from instrument coordinates to physical coordinates $\mathbf{Q}$, E, using algorithms implemented in Mantid analysis software [2]. All data were normalized and corrected by a standard vanadium sample. The data were grouped into Q bins of width $0.2\,\text{Å}^{-1}$ with center ranging from 0.3 to $1.9\,\text{Å}^{-1}$. The suppression of the QENS peak height arises because the elastic intensity decreases upon heating due to the large Debye-Waller factor of the mobile Li^+ sublattice. The reversibility is checked after cooling back to 300 K and gives the same spectra as the one before heating, which confirms that the sample remain intact after heating to 680 K.

The model scattering function we used to fit the QENS data can be written as:

$$I(Q,\omega) = \left[A\delta(\omega-\omega_0) + B\frac{1}{\pi}\frac{\Gamma(Q)}{\Gamma^2(Q)+(\omega-\omega_0)^2}\right] \otimes R(Q,\omega) + BG(Q) \quad (6)$$

where the scattering intensity $I(Q,\omega)$ is fitted with an elastic line (δ function), a quasielastic peak (Lorentzian function) convoluted with the sample depenedent instrument resolution function $R(Q,\omega)$, and a linear background $BG(Q)$. A, B are constants.

The polycrystalline samples need to be hold in a container, e.g., an ampoule or a standard aluminum can. A measurement of the empty container at the identical condition is required to extract the true signal from the sample:

$$I_{sample} = I_{raw} - \xi \cdot I_{emptycan} \quad (7)$$

where ξ is the self-shielding factor, normally < 1. This factor is applied because the scattering condition will change when sample is placed in the container. The value of ξ can be determined by checking the residue of the diffraction pattern from the sample holder after the subtraction.

The fitted half-width at half-maximum Γ (HWHM) at each temperature is fitted with a jump-like diffusion Chudley-Elliot (CE) model [3]:

$$\Gamma(Q,\omega) = \frac{1}{\tau}\left(1 - \frac{sin(Qd)}{Qd}\right) \quad (8)$$

where d and τ are the average jump-length and the residence time. At the low-Q limit, the variance of $\Gamma(Q)$ can be used to extract the coefficient:

$$D = d^2/6\tau \quad (9)$$

Although the $^7Li_6PS_5Cl$ are found to be less air sensitive compared to other LISICONs, the moisture can cause its decomposition. Thus, the samples were sealed in preheated quartz ampoules under vacuum as written in the synthesis section. Additional aluminum foil and sample can is used to properly mount the sample to the instrument, as shown in Fig. **??**. This unconventional setting adapted in this experiment results in a complex scattering environment compared to conventional flat cell geometry. The elastic peak intensity is used to evaluate a proper empty can factor ξ (Equ. 7). In this case, we assume the raw signal has extra scattering of the empty can compared to the intrinsic sample signal. As can be seen in Fig. **??**, $\xi = 1$ results in a negative subtraction, meaning the empty can has more scattering compared to the case with $^7Li_6PS_5Cl$. The extra scattering could originate from the absorption from Cl^-, and due to uneven setting between the sample and empty can. Nevertheless, a correction factor of $\xi = 0.75$ shows proper correction in the following analysis process as we will show later.

Inelastic Neutron Scattering: INS measurements were performed with the same powder samples as BASIS using ARCS [4]. In the ARCS measurements, we used a top-loading closed-cycle refrigerator with a hot stage. Incident energy $E_i = 180$ meV was used to cover the whole phonon energy range and $E_i = 25$ and 50 meV render finer resolution to capture the details of the low-energy phonon modes. Data were collected at the same temperature as BASIS from 100 to 680 K. The Fermi chopper and the t-zero chopper were on automatic modes. These configurations provided an estimated elastic line energy resolution of 0.96 meV at $E_i = 25$ meV, 1.80 meV at $E_i = 50$ meV and 10.14 meV at $E_i = 180$ meV. An oscillating radial collimator was used, and the empty can background scattering data were collected with an identical configuration as sample measurement. $S(E)$ is summed over the whole Q-range. The analysis of phonon density of state (DOS) was performed within the incoherent scattering approximation. Corrections for multiphonon and multiscattering were applied as detailed in Ref. 5. The elastic peak region ($E < 1.5$ meV) for $E_i = 25$ meV was removed. No

extrapolation was included due to the non-Debye dynamics from superionic Li^+ diffusion. The neutron-weighted DOS is expressed as:

$$\begin{aligned} g(\omega) &= \sum_i f_i \frac{\sigma_i}{m_i} g_i(\omega) \\ g_i(\omega) &= \sum_{j,\mathbf{q}} |e_i(j,\mathbf{q})|^2 \delta(\omega - \omega(j,(q))) \end{aligned} \tag{10}$$

where f_i, σ_i, m_i and $g_i(\omega)$, $e_i(j,\mathbf{q})$, $\omega(j,\mathbf{q})$ are the atomic fraction, neutron total cross-section, atomic mass, partial density of states, phonon eigenvectors and phonon frequencies of atom i. We weighted the simulated DOS with the neutron cross-sections so that it can be directly compared with the experimentally measured DOS.

DFT, AIMD, and MLMD simulations: Theoretical calculations were performed with the Vienna *Ab initio* Simulation Package (VASP 5.4) [6–8], using the PBE exchange-correlation functional [9, 10]. The cubic unit cell consists of 52 atoms with a lattice constant of 9.859 Å. 24 Li^+ are removed randomly to ensure the stoichiometry of the 50% occupancy. 50% disorder of Cl^-/S^{2-} is also randomly generated. A 2×2×2 k-point mesh with a plane-wave cut-off energy of 500 eV was used. The electronic self-consistent loop convergence was set to 10^{-6} eV.

Ab initio molecular dynamics (AIMD) simulations were performed using NVT-ensemble with Nosé–Hoover thermostat from 100 to 800 K with 100 K steps. Each simulation trajectories were 2 ps long with a time step of 2 fs to sample the potential energy surface. Longer trajectories at 200 and 600 K of 20 ps with 2×2×1 were calculated to validate against MLMD trajectories.

We used DeePMD-kit code [11] to train a surrogate neural-network force-field based on machine learning. The surrogate force-field was validated against reference AIMD data, including out-of-distribution tests with larger cell size than the training data (Fig. **??**). Dynamic properties were also benchmarked against AIMD (Fig. **??**-**??**).

MLMD simulations were performed with LAMMPS [12] on 3×3×3 supercell (1404 atoms) with NVT and NPT ensembles. Calculations were done with both the experimental lattice parameters and NPT relaxed lattice parameters at specific temperature. Temperature and pressure were controlled by Nosé-Hoover thermostat and barostat with time constant 0.1 ps and 1 ps. For QENS calculation, the trajectory is $\sim$ 1 ns long which gives an energy resolution of 3.2 μeV, and momentum resolution $\sim$ 0.2 $Å^{-1}$. Constraint calculation were performed on 2×2×2 supercell (416 atoms). Unconstraint case at two supercells were tested first which yields the same MSD. Five constraint cases are considered in MLMD: (i) making PS_4^{3-} units rigid bodies (green diamonds) that can rotate or translate as a whole; (ii) rigid PS_4^{3-} units with frozen rotations (brown triangles), only allowing translational vibrations ("wiggling"); (iii) fixing S and P ions in PS_4^{3-} units to their initial positions (blue pentagons), while free S, Cl and Li ions are mobile; (iv) fixing positions of all free S and Cl ions (pink hexagons); (v) fixing all framework ions (P, S, Cl), with only Li^+ mobile (black crosses). For $S(\mathbf{Q},\omega)$ calculations of low energy phonons, we used 2×2×20 supercell (4160 atoms) for the longitudinal mode along 00L, which give commensurate $\mathbf{Q}$ of 0.1 in reciprocal lattice unit (r.l.u.) along the 00L direction. For TA phonons along 0H0, we used 2×10×10 supercell (10400 atoms), which give commensurate $\mathbf{Q}$ of 0.2 r.l.u., in all directions. Three parallel trajectories are averaged to improve the statistics of the data.

The mean square displacement (MSD), is calculated to extract the diffusion coefficient from MLMD:

$$< u_i^2(t) >= \frac{1}{N} \sum_{i=1}^{N_i} \langle |r_i(t) - r_i(0)|^2 \rangle \tag{11}$$

where N_i is the number of atoms, $r_i(t)$ is the position of the ith atom at time t. <> represents the ensemble average. The self-diffusion coefficient is estimated using Einstein relation over a period τ:

$$D_i(T) = \frac{< u_i^2(\tau) >}{6\tau} \tag{12}$$

The total neutron scattering intensity is the sum of the coherent and incoherent components [13]:

$$I(Q,\omega) \propto \sum_{i,j} b_{coh}^i b_{coh}^j S_{coh}^{ij}(Q,\omega) + \sum_j b_{inc}^{j^2} S_{inc}^j(Q,\omega) \tag{13}$$

where b_{coh}^i and b_{inc}^i are the coherent and incoherent scattering length of the i^{th} atoms. For Li, $\sigma_{coh}^{7Li} (= 4\pi b_{coh}^2) =$ 0.619 barn and $\sigma_{inc}^{7Li} (= 4\pi b_{inc}^2) =$ 0.78 barn, thus, both contributions should be considered. The coherent scattering measures the space-time correlations between a pair of atoms, which probes a correlated diffusion process. The incoherent scattering measures the time correlation of the positions of a single atom (self-diffusion) [14, 15]. As can be seen in Fig. **??**, the incoherent scattering of Li^+ dominates the QENS signal whose width increases with Q, matching the observations in our neutron measurements, whereas the coherent scattering has almost negligible contribution to the QENS broadening and remain constant above 5 μeV (except for phonon excitation at meV energies). This establishes that the Li^+ self-diffusion generates the QENS signal. Concerted motions of multiple ions such as lithium cage rearrangements are possible, as simulated in Ref. [16], which would show up in the (weak) coherent scattering signal. The simulated $S_{inc}^{Li}(Q,\omega)$ is fitted with two Lorentzians to distinguish the different timescales for inter-cage and intra-cage/doublet hops (elastic line excluded).

DATA AND CODE AVAILABILITY

All data that support the conclusion of this work are available from the corresponding author upon reasonable request. The numerical data for the figures

are available from the Harvard Dataverse Repository at https://doi.org/10.7910/DVN/RCBK4U. The codes that support findings of the study are available from the corresponding author upon reasonable request.

METHODS-ONLY REFERENCES

[1] Eugene Mamontov and Kenneth W Herwig. A time-of-flight backscattering spectrometer at the spallation neutron source, basis. Review of Scientific Instruments, 82(8):085109, 2011.

[2] O Arnold, J C Bilheux, J M Borreguero, A Buts, S I Campbell, L Chapon, M Doucet, N Draper, R Ferraz Leal, M A Gigg, V E Lynch, A Markvardsen, D J Mikkelson, R L Mikkelson, R Miller, K Palmen, P Parker, G Passos, T G Perring, P F Peterson, S Ren, M A Reuter, A T Savici, J W Taylor, R J Taylor, R Tolchenov, W Zhou, and J Zikovsky. Mantid—Data analysis and visualization package for neutron scattering and μSR experiments. Nuclear Instruments and Methods in Physics Research Section A: Accelerators, Spectrometers, Detectors and Associated Equipment, 764:156–166, November 2014.

[3] CT Chudley and RJ Elliott. Neutron scattering from a liquid on a jump diffusion model. Proceedings of the Physical Society (1958-1967), 77(2):353, 1961.

[4] D L Abernathy, M B Stone, M J Loguillo, M S Lucas, O Delaire, X Tang, J Y Y Lin, and B Fultz. Design and operation of the wide angular-range chopper spectrometer ARCS at the Spallation Neutron Source. Review of Scientific Instruments, 83(1):015114, 2012.

[5] YY Lin, Fahima Islam, and Max Kresh. Multiphonon: Phonon density of states tools for inelastic neutron scattering powder data. Journal of Open Source Software, 3(21), 2018.

[6] G Kresse and J Hafner. Ab initio molecular dynamics for liquid metals. Physical Review B, 47(1):558–561, January 1993.

[7] G Kresse and J Furthmüller. Efficient iterative schemes for ab initio total-energy calculations using a plane-wave basis set. Physical Review B, 54(16):11169–11186, October 1996.

[8] G Kresse and J Furthmüller. Efficiency of ab initio total energy calculations for metals and semiconductors using a plane-wave basis set. Computational Materials Science, 6(1):15–50, July 1996.

[9] J.P. Perdew and A. Zunger. Self-interaction correction to density-functional approximations for many-electron systems. Physical Review B, 23:5048–5079, 1981.

[10] J.P. Perdew, K. Burke, and M. Ernzerhof. Generalized gradient approximation made simple. Physical Review Letters, 77:3865–3868, 1996.

[11] Han Wang, Linfeng Zhang, Jiequn Han, and E Weinan. Deepmd-kit: A deep learning package for many-body potential energy representation and molecular dynamics. Computer Physics Communications, 228:178–184, 2018.

[12] A. P. Thompson, H. M. Aktulga, R. Berger, D. S. Bolintineanu, W. M. Brown, P. S. Crozier, P. J. in 't Veld, A. Kohlmeyer, S. G. Moore, T. D. Nguyen, R. Shan, M. J. Stevens, J. Tranchida, C. Trott, and S. J. Plimpton. LAMMPS - a flexible simulation tool for particle-based materials modeling at the atomic, meso, and continuum scales. Comp. Phys. Comm., 271:108171, 2022.

[13] Mayanak K Gupta, Jingxuan Ding, Naresh C Osti, Douglas L Abernathy, William Arnold, Hui Wang, Zachary Hood, and Olivier Delaire. Fast na diffusion and anharmonic phonon dynamics in superionic na 3 ps 4. Energy & Environmental Science, 14(12):6554–6563, 2021.

[14] Stephen W Lovesey. Theory of neutron scattering from condensed matter. 1984.

[15] Tasso Springer. Quasielastic neutron scattering for the investigation of diffusive motions in solids and liquids. Springer Tracts in Modern Physics, Volume 64, pages 1–100, 2006.

[16] Benjamin J Morgan. Mechanistic origin of superionic lithium diffusion in anion-disordered li6ps5 x argyrodites. Chemistry of Materials, 33(6):2004–2018, 2021.

Liquid-like dynamics in a solid-state lithium electrolyte

Jingxuan Ding,[1,2] Mayanak K. Gupta,[1,3] Carolin Rosenbach,[4] Hung-Min Lin[5]
Naresh C. Osti,[6] Douglas L. Abernathy,[6] Wolfgang G. Zeier,[4,7] Olivier Delaire [1,5,8*]
[1] *Department of Mechanical Engineering and Materials Science, Duke University, Durham, NC 27708, USA*
[2] *John A. Paulson School of Engineering and Applied Sciences, Harvard University, Cambridge, MA 02138, USA*
[3] *Solid State Physics Division, Bhabha Atomic Research Centre Mumbai, Maharashtra 400085, India*
[4] *Institute of Inorganic and Analytical Chemistry, University of Münster, Münster D-48149, Germany*
[5] *Department of Chemistry, Duke University, Durham, North Carolina 27708, USA*
[6] *Neutron Scattering Division, Oak Ridge National Laboratory, Oak Ridge, Tennessee 37831, USA*
[7] *Institute of Energy Materials and Devices (IMD), IMD-4: Helmholtz-Institut Münster, Forschungszentrum Jülich, Münster 48149, Germany*
[8] *Department of Physics, Duke University, Durham, North Carolina 27708, USA*
[*] *To whom correspondence should be addressed; E-mail: olivier.delaire@duke.edu*

Superionic materials represent a regime intermediate between the crystalline and liquid states of matter. Despite the considerable interest in potential applications for solid-state batteries or thermoelectrics, it remains unclear whether the fast ionic diffusion observed in superionic materials reflects liquid-like dynamics or whether the hops of mobile ions are inherently coupled to more conventional lattice phonons. Here, we reveal a crossover from crystalline vibrations to relaxational dynamics of ionic diffusion in the superionic compound Li_6PS_5Cl, a candidate solid-state electrolyte. By combining inelastic and quasielastic neutron scattering measurements with first-principles based machine-learned molecular dynamics simulations, we find that the vibrational density of states in the superionic state strongly deviates from the quadratic behavior expected from the Debye law of lattice dynamics. The superionic dynamics emerge from overdamped phonon quasiparticles, giving rise to a linear density of states characteristic of instantaneous normal modes in the liquid state. Further, we show that the coupling of lattice phonons with a dynamic breathing of the Li^+ diffusion bottleneck enables an order-of-magnitude increase in diffusivity. Thus, our results shed new insights into superionics for future energy storage and conversion technologies.

Superionic conductors (SICs) are materials intermediate between the crystalline and liquid states of matter, and their unusual behavior has attracted fundamental interest for decades [1–3]. While retaining a partly crystalline character, SICs develop upon warming a sublattice of delocalized mobile ions with diffusivities comparable to those of liquids [1, 2]. They are attracting strong interest for their potential in applications such as solid-state batteries or thermoelectrics, yet their atomic structure and dynamics remain poorly understood. In crystals, harmonic phonons represent small-amplitude collective oscillations of atoms around an energy minimum at THz frequencies, propagating through the periodic lattice as quasiparticles, which successfully account for many thermodynamic and transport properties [4–6]. However, harmonic phonons are not *a priori* suited to describe complex dynamics in many condensed matter phases with strong disorder and large dynamical displacements, such as amorphous solids, liquids, or rotor phases and SICs.

Fundamentally different dynamics in these more complex phases are reflected in the violation of the Debye-law for the vibrational density of state (DOS) normally obeyed by crystalline solids: $g(\omega)\sim\omega^2$ at low frequency ω. In liquids, negative curvatures in the potential energy surface around intermittent local environments cause the phonon description to lead to a high density of modes with unphysical imaginary frequencies [7]. These so-called instantaneous normal modes (INMs) [8, 9] are manifested via anharmonic overdamped spectral responses that lead to a universal linear law for the DOS, $g(\omega)\sim\omega$ [10]. In amorphous solids, soft localized modes following another non-Debye scaling law [$g(\omega)\sim\omega^4$] are observed at low ω [11].

In SICs, the low-frequency behavior of $g(\omega)$ remains to be determined, an important point to assess their liquid-like vs solid-like nature. In addition, it is unclear to what extent the phonon-like dynamics expected for the crystalline framework couples with the hopping of ions on the mobile sublattice of the compound structure. To describe the hybrid dynamics of SICs in a unified approach, we adopt a conceptual framework beyond that of traditional quasiharmonic phonons, and consider the regime of overdamped spectra, guided by INMs in liquids.

While some observations of phonon quasiparticle breakdown have been reported in SICs [12–17], phonon modes derived from the parent crystalline lattice could still provide a convenient framework to glean insights into key diffusion steps around an ionic configuration, potentially serving as descriptors or enablers of fast diffusivity. Indeed, prior investigations of SICs and solid-state electrolytes established correlations of the enthalpy of migration (hopping barrier) with the low optical phonon frequencies or lower Debye and mean phonon frequencies

[18–21], and also correlated diffusion pre-factors with averaged lithium phonon frequencies [22, 23]. Vibrational and anharmonic characteristics were also recently considered as descriptors in a data-driven study [24].

From an applied perspective, the demand for rechargeable batteries with higher energy density, improved safety and reliability is driving the search for SICs with high lithium ion conductivity σ [25–28]. Sulfide solid-state electrolytes are among the most promising candidates thanks to high ionic conductivity comparable to liquid electrolytes, for instance $Li_{10}GeP_2S_{12}$ [29], $Li_{9.54}Si_{1.74}P_{1.44}S_{11.7}Cl_{0.3}$ [30], and argyrodite $Li_{5.5}PS_{4.5}Cl_{1.5}$ [31, 32] ($\sigma \sim$10−25 mS·cm^{-1}). The high σ of sulfide solid-state electrolytes has been associated with their soft lattice and highly polarizable S^{2-} anions, suggesting an underlying connection between fast diffusion and host lattice phonons [16, 20–22, 33–36], yet the role of phonons has remained difficult to ascertain owing to the highly complex structures and dynamics characteristic of solid-state electrolytes.

Here, we report important new insights by considering both strongly anharmonic phonon-derived vibrations of the crystalline lattice and stochastic hopping dynamics of the mobile Li^+ in Li_6PS_5Cl. To this end, we performed inelastic and quasielastic neutron scattering (INS and QENS), density functional theory and ab initio molecular dynamics (AIMD) simulations, augmented with machine-learning (MLMD), to reach nanosecond time-scales and to isolate key degrees-of-freedom. We uncover extreme damping and breakdown of soft anharmonic phonons associated with Li^+ motions, revealed in a low-energy spectral-weight enhancement. The signal follows the linear $g(\omega)\sim\omega$ characteristic of liquids and constitutes a signature of Li^+ hopping through extended anharmonic regions of the potential energy surface, disrupting long-range periodicity. It occurs concurrently with the enhanced QENS width that directly probes diffusivity, highlighting the intrinsic connection between low-energy vibrational and diffusive dynamics. We also establish the importance of phonons of the crystalline framework, showing how they enhance Li^+ diffusivity by an order of magnitude at ambient temperature. Vibrations of PS_4^{3-} are critical in opening up the structural bottleneck for long-range diffusion, while little effect of rotations ("paddle-wheel" mechanism) is observed. The picture emerging from our experiments and simulations bridges conventional diffusive and lattice vibrational models. Superseding simple quasiharmonic approximations and parametrizations in terms of averaged Li^+ vibrational frequencies [22, 23]. This picture extends pioneering connections between low energy phonon modes and ionic diffusion [18, 37] by integrating the concept of overdamped spectral functions associated with strongly anharmonic INMs [10, 38].

Spectral evolution from soft phonons to fast Li^+ diffusion

Non-Debye dynamics from superionic Li^+ diffusion:

We first reveal the emergence of non-Debye like behavior of $g(\omega)$ at low-ω in Li_6PS_5Cl upon warming. As shown in Fig. 1 (c), at 100 K, two phonon peaks are observed in the dynamical structure factor $S(E)$ ($E = \hbar\omega$) around 8 and 15 meV, but upon warming, the overall intensity increases with phonon occupations, and above 400 K, a clear quasielastic broadening develops around the elastic line, below $E < 4$ meV. This indicates a characteristic signal from fast intra-cage/doublet hops (the diffusion path is discussed later), and is reminiscent of spectral weight transfers observed in SICs with much heavier mobile cations (Ag^+, Cu^+ or Na^+) [12, 13, 16]. Strong softening and broadening for both peaks are observed, indicating phonon frequency renormalizations and enhanced phonon scattering rates as in a damped harmonic oscillator:

$$S(E) \propto (n + \frac{1}{2} \pm \frac{1}{2}) \frac{\Gamma E}{(E - E_0^2)^2 + (\Gamma E)^2} \qquad (1)$$

where Γ is the phonon linewidth and E_0 the undamped phonon frequency. The phonon DOS at 100 and 200 K extracted from INS exhibit a conventional Debye-like quadratic DOS at low frequency [$g(\omega) \sim \omega^2$], consistent with collective quasiharmonic dynamics of ions vibrating near the bottom of local potential minima [Fig. 1 (d,f)], see blue dashed line fit. However, at 600 K a qualitatively different regime emerges with a linear behavior (red dashed line). Note also that a small but finite spectral weight is expected to develop at $\omega = 0$. This represents diffusion, and will be discussed in more detail later. The linear and quadratic fits of $g(\omega)$ at other temperatures are summarized in Fig. S4 and Table. S1. For clarity, we emphasize that we are here referring to the Debye model of lattice dynamics, which describes collective atomic vibrations in a crystal with quantized normal modes (phonons) [40, 41]. This is distinct from the Debye equation describing the relaxation response of a dielectric medium in an external oscillating electric field [42–44].

The linear DOS $g(\omega) \sim \omega$ was recently derived from the Green's function as a universal response of liquids for a collection of INMs j [10]:

$$g(\omega) = \frac{1}{3\pi N} \sum_j \frac{\omega}{\omega^2 + \Gamma_j^2} \qquad (2)$$

where N is the total number of atoms, Γ_j is the relaxation rate of the jth INM, similar to the above phonon linewidth. A linear dependence results in the low frequency limit of overdamped INMs $\omega << \Gamma_j$:

$$g(\omega) = \alpha\omega + O(\omega^3),\ \alpha = \sum_j \frac{1}{3\pi N \Gamma_j^2} \qquad (3)$$

In addition to non-Debye behavior, the INS data in Fig. 1 (d) show a clear excess in spectral weight at low E. Figure 1 (e) shows a zoomed view of DOS curves without any vertical offset at 200 K and 600 K, obtained from INS (top panel) and MLMD (bottom panel). Extra intensity

is seen in spectrum at 600 K compared to 200 K (grey shaded area). Simulations reveal the predominant contribution of Li^+ dynamics in this excess spectral weight (dashed lines). Details in the temperature dependent spectra are discussed in Supplementary Information section 1.

A direct proportionality between the diffusion coefficient and the zero-energy limit of the spectral density, $g(\omega \to 0)$, can be derived from the velocity autocorrelation function $\langle v(0) \cdot v(t) \rangle$ (see Supplementary Information section 2 for derivations):

$$D = \frac{1}{3} \int_{-\infty}^{\infty} \langle v(0) \cdot v(t) \rangle dt \tag{4}$$

$$g(\omega) = \frac{1}{2\pi} \frac{\int_{-\infty}^{\infty} \langle v(0) \cdot v(t) \rangle e^{-i\omega t} dt}{\langle v(0) \cdot v(0) \rangle} \tag{5}$$

We estimate D=7.52×10^{-6} cm^2/s from MLMD $g(\omega \to 0)$ at 600 K, closely matching the values from both QENS and MLMD (see below). The corresponding values for $g(\omega \to 0)$ are 1.03±0.43 and 0.63±0.27 meV^{-1} for QENS and INS, respectively. Thus, both our experimental and computational probes of the low-E range of the THz spectrum (1 THz = 4.136 meV) let us identify the fast ionic hopping process. In fact, due to the fixed number of degrees-of-freedom, the breakdown of vibrational modes reflects the spectral weight transfer from local oscillation to diffusion.

Li^+ diffusion with QENS and MLMD

Crystal structure and diffusion path: Next, we investigate the Li^+ diffusion path and associated time-scales through combined QENS, INS and simulations. Lithium argyrodites have the general composition Li_7PnCh_6, where Pn = P or As and Ch = O, S, Se can be replaced with halogens (X), as in Li_6PS_5X (X = Cl, Br, I) [32]. Fig. 1 (a) shows the unit cell of Li_6PS_5X (space group $F\bar{4}3m$). At low-T, Li^+ mainly occupy Wyckoff 48h sites (T5) surrounding the 4c S^{2-}, and partly 24g (T5a) and type 2 (T2) with overall 50% occupancy, as shown from our MLMD computation of Li^+ probability (Fig. **??**). This is in agreement with neutron diffraction measurements [45]. Arrows in Fig. 1 represent the three hopping processes defined in Refs. 16, 46. The actual hops occur through intermediate sites, namely: (i) doublet hops (T5-T5a-T5); (ii) intra-cage hops (T5-T2-T5); and (iii) inter-cage hops (T5-T2-T2-T5) [20, 45, 48]. The inter-cage hopping rate is an order-of-magnitude lower than the other rates, and is thus the bottleneck for long-range diffusion. These processes are confirmed by the computed Li^+ probability distribution from MLMD at 600 K [Fig. 1 (b)]. A proposed T1x site [49] is not observed in our simulations, however (detailed in Supplementary Information section 3). Below, we will clarify the atomistic mechanisms enabling fast Li^+ diffusion, and isolate key host vibrational modes.

Resolving multiple hopping timescales: We determine the diffusion coefficient from QENS data, shown in Fig. 2 (a). The central peak broadening beyond the intrinsic instrument resolution [Fig. S7] is a Lorentzian signature of ionic diffusion [50], see *e.g.,* 400 K *vs* 300 K. Based on our MLMD simulations [Fig. S11], the slow signal below 0.1 meV corresponds to the bottleneck inter-cluster hops, and the faster intra-cluster hops contribute to the linear DOS region observed in INS. A typical fit of QENS data (T = 600 K, Q = 1.5±0.1 Å^{-1}) is shown in Fig. 2 (b), consisting of three terms: elastic intensity (delta function), QENS (Lorentzian), and a linear background. The Lorentzian half-width at half-maximum (HWHM) increases with momentum transfer Q and plateaus around 1.5 Å^{-1}. This behavior is expected for jump diffusion on a lattice and is captured well by a Chudley-Elliot model, as shown in Fig. 2 (c). From this, we can extract a diffusion coefficient D, jump length d and residence time τ (see Methods). At 600 K, the estimated inter-cage hopping coefficient is D=(5.0±2.1)×10^{-6} cm^2/s, in good agreement with reported MD simulations of long-range diffusion. A detailed summary of diffusion coefficients and activation energies from previous references is provided in Supplementary Information section 4. At 300 K, D=(0.7±0.2)×10^{-6} cm^2/s lies in the range of the reported values from impedance measurements (10^{-9} to 10^{-5} cm^2/s). D increases and τ decreases with increasing temperature (Fig. S8), and an activation energy of 0.11 eV can be estimated from the Arrhenius fit of D *vs* T. This value is smaller than estimates from nuclear magnetic resonance for long-range diffusion, which lie in the range of 0.132 to 0.35 eV, or the values of 0.16 to 0.45 eV from electrochemical impedance spectroscopy. While both QENS and nuclear magnetic resonance probe microscopic ionic conduction, a higher E_a value in nuclear magnetic resonance measurements is a common observation across various systems. The larger values inferred from impedance measurements could originate from boundary and contact resistances, or voids in samples.

To resolve the distinct timescales between the slow inter-cage hops and the ten-times faster intra-cage/doublet hops, we directly simulate the neutron spectra with MLMD trajectories over 1 ns (3.2 μeV energy resolution), and approaching the experimental resolution of 3.5 μeV at BASIS. Importantly, the simulated spectra consist of two Lorentzians, one below 0.1 meV and one around 1 meV (Fig. S10). The narrower component reflecting less-frequent inter-cage hops is in excellent agreement with QENS [Fig. 2 (b)]. The corresponding diffusion coefficients from QENS and MLMD are 5.0×10^{-6} and 6.6×10^{-6} cm^2/s, respectively and the jump lengths (d_{jump} = 2.4±0.4 Å and 2.7±0.1 Å) match the crystallographic inter-cage hopping distance. The wider spectral component, corresponding to the fast intra-cage/doublet hops, has a ten-times larger width and thus ten-times shorter τ (Table. I). The estimate for fast processes is an average of intra-cage

and doublet hops, thus leading to a larger uncertainty in the corresponding D, and the estimated d_{jump} = 1.2±0.1 Å is the average of the T5-T5a (0.8 Å) and T5-T2 distances (1.5 Å) [Fig. 1 (b)]. Moreover, the HWHM from QENS measurement at large $|\mathbf{Q}|$ (e.g., $|\mathbf{Q}|$=1.5 Å) is 87.4±2.7 μeV at 600K. If this QENS signal resulted from fast intra-cage hopping, then an order-of-magnitude narrower component from a slower process would be expected, and could still be resolved (the BASIS resolution is 3.5 μeV), but such a slow component is not observed. Hence, this QENS broadening must be contributed by inter-cage hopping. This is also consistent with the MLMD estimated QENS width from inter-cage hopping. Further, the diffusion coefficient is also estimated from the computed window-averaged mean square displacements (MSD) *vs* time via the Einstein formula (trajectory lengths over 500 ps, Fig. S7). Our MSD calculations quantitatively agree with the AIMD simulation at 500 K in Ref. 16. An Arrhenius fit provides an activation barrier of 0.16 eV, close to the value of 0.11 eV from QENS, also in good agreement with the values of 0.18 eV from AIMD in Ref. 51. Thus, combining QENS experiments and simulations, we fully resolved the spatial and temporal characteristics of the complex diffusion process in Li_6PS_5Cl, benchmarking our MLMD approach. Finally, we further analyzed the diffusive dynamics by tallying all inter-cage hops in the MLMD trajectories (detailed in Supplementary Information section 5). Spherical cage boundaries were defined with respect to a central S or Cl ion at Wyckoff 4*c* sites [Fig. S16 (b)] and used to identify Li^+ inter-cage jumps. Accounting for all jumps in 19 parallel nanosecond-long MLMD simulations at 600K, we obtained average Li^+ inter-cage hopping timescales (mean cage residence time) of 24, 37, and 51 ps for cage radii of 4.0, 3.75, 3.5 Å, respectively. These results are in good agreement with the residence time from our Chudley-Elliot fits in Table. I. Our estimate of hopping timescale agrees well with the AIMD results of Klerk et al [46]. Deviations may originate from the larger unit cell and longer simulation used in our MLMD, which provides better statistics. It is expected that smaller spherical cages miss some inter-cage jumps as they do not account for the whole region connecting cages..

Facile Li^+ diffusion from anharmonic phonons

Evolution from vibrational to diffusive dynamics: Examining the neutron-weighted spectra from MLMD in Fig. S3, we see that the Li spectral weight originally at high energy (>25 meV) shifts toward lower frequencies on warming, while only a slight broadening occurs for S, P, and Cl spectra. Surprisingly, as the diffusion coefficients increased by 300× from 200 K to 600 K (0.0522×10^{-6} to 15.9×10^{-6} cm^2/s), the averaged Li band center only softened by −5% (33.56 to 32.04 meV). However, the low-E (<10 meV) Li spectral intensity is much more sensitive, and increases by 60%. Furthermore, comparing vibrational spectra from MLMD with various constraints [Fig. 3 (c) and S6], we find that the suppression of high energy modes is not critical for fast ionic diffusion. The humps at 30, 50, and 60 meV are associated with internal motions of the PS_4^{3-} unit, which vanish for rigid PS_4^{3-}, while the rotational modes of PS_4^{3-} contribute strongly at 20 meV. High energy modes involving Li^+ motions show some variation around 50 meV, which may be related to the vibrations of S in PS_4^{3-}. A recent study suggested that low-E polyanion rotational modes couple with these high-E Li modes and are less important for Li^+ diffusion [52]. The largest effect occurs below 10 meV, and the value of $g(\omega \to 0)$ is finite in all the cases featuring fast diffusion, following the estimated diffusion coefficients from MSD. Strikingly, in the case of fixed PS_4^{3-} and fixed host, the spectral weight below 10 meV is strongly suppressed [Fig. 3 (c)], which concurs with the abrupt decrease in the diffusion coefficient.

Dynamic breathing of the structural bottleneck: We now probe the correlation of Li^+ diffusion with the flexibility of the argyrodite structure. In Fig. 3 (a,b), we compare trajectories of a specific Li^+ over 500 ps, computed from MLMD without constraints or with fixed host, respectively. The unconstrained trajectory shows long-range Li^+ diffusion spanning multiple different cages and containing more than ten inter-cage jumps (see also Fig. **??**). Interestingly, the Li^+ ion in Fig. 3 (a) explores each cage (green segments) for a relatively long time, yet inter-cage hops occur very fast, within 0.5 ps (red segments). In contrast, inter-cage hops are strongly suppressed when the host framework is fixed [Fig. 3 (b)]. Therefore, the host lattice vibrations play a crucial role in enabling long-range diffusion. Additional examples of trajectories for both cases are shown in Fig. S14, S15. To gain a finer understanding of this process, in Fig. 3 (c) inset, we zoom in on the structural bottleneck between adjacent T5-T2 and T2-T2 sites (see also Fig. S22, S23 and Supplementary Information section 6). The time-averaged bottleneck area exhibits a wider distribution when unconstrained. This shows the importance of dynamic breathing of the structural bottleneck for Li^+ diffusion. The trends in dynamic breathing also highlight the anharmonic nature of the potential. The interatomic potential energy surface is anharmonic and shallow, "frustrated" in the sense that there is not a single deep locally-harmonic minimum in the configurational space. The thermal energy at 600 K already allows Li^+ to explore wide swaths of this shallow surface along its diffusion path.

Overdamped vibrational regime: We further investigate the spectral functions of specific phonon modes and evaluate their broadening in the superionic regime. From MLMD trajectories, we calculated the momentum-resolved dynamical susceptibility, $\chi''(\mathbf{Q},\omega)$, shown in Fig. 3 (d-f) (see Supplementary Information section 7). We find that the longitudinal-polarized phonons are

already very broad (anharmonic) at 50 K but broaden even more at 600 K. The transverse-polarized phonons near the zone boundary, where a dominant contribution from Li^+ is expected, completely break down into an overdamped response [Fig. 3 (f)]. This behavior is consistent with overdamped INM behavior and is reminiscent of observations in Ag^+ [13] or Na^+ conductors [53].

Identifying key host vibrations: To resolve the host vibrations that most strongly affect Li^+ diffusion, we implemented five different constraints in MLMD: (i) making PS_4^{3-} units rigid bodies (green diamonds) that can rotate or translate as a whole; (ii) rigid PS_4^{3-} units with frozen rotations (brown triangles), only allowing translational vibrations ("wiggling"); (iii) fixing S and P ions in PS_4^{3-} units to their initial positions (blue pentagons), while free S, Cl and Li ions are mobile; (iv) fixing positions of all free S and Cl ions (pink hexagons); (v) fixing all framework ions (P, S, Cl), with only Li^+ mobile (black crosses). As shown in Fig. 2 (d), we clearly see that making PS_4^{3-} units rigid (constraint i) minimally impacts D. Further, comparing cases (ii) (wiggling-only) *vs* (iii) (fixed PS_4^{3-}) shows that wiggling of PS_4^{3-} is more conducive to Li^+ diffusion (see brown *vs* blue markers). This agrees with a MD investigation of $Na_{3-x}Sb_{1-x}W_xS_4$ [54]. Recently, polyhedral anion rotations and re-orientations in so-called "rotor" or "plastic" phases have attract particularly strong interest in solid-state electrolytes [55–57]. However, full re-orientations of PS_4^{3-} are not observed in our MLMD at 600 K (Fig. S20). We find rotations of limited amplitudes, similar to prior results in a Cu-based argyrodite [16]. Our observations are consistent with a recent report that attributes fast diffusion to an occupancy-change-driven tilting (soft-cradle effect), rather than a paddle wheel effect [58]. The angular autocorrelation function averaged over all P-S pairs was further analyzed at 300 and 600 K [Fig. S20 (d) and Supplementary Information section 8], which shows the lack of PS_4^{3-} reorientations (self-correlated P-S bond direction). The small decrease at 600 K is ascribed to larger-amplitude atomic vibrations.

When all framework ions are immobilized, the rigid bottleneck strongly constrains Li^+ diffusion [Fig. 2 (d)]. This is further corroborated through an analysis of fluctuations of the bottleneck cross-sectional areas, shown in Fig. S22. Unlocking host dynamics enables wider-amplitude fluctuations and facilitates inter-cage diffusion. Importantly, our results show that the host vibrations modulate the diffusion coefficient by $\sim 10\times$ at room temperature, even in a soft polarizable material already including compositional disorder. We note that such effects could be missed if performing only high-T MD simulations. At 600 K, the enhancement is more modest ($\sim 3\times$) because the thermal energy already allows Li^+ to explore wider regions of the interatomic potential energy surface.

CONCLUSION AND OUTLOOK

In summary, we integrated neutron scattering and machine-learning augmented first-principles simulations to gain new insights into the complex atomic dynamics of the solid-state electrolyte Li_6PS_5Cl, revealing a crossover from phonon quasiparticles typical of crystals toward the relaxational behavior and intrinsic normal modes characteristic of liquids. These insights into the microscopic mechanism of fast Li^+ diffusion in argyrodites could guide the design of future materials for solid-state electrolytes. In the superionic regime, Li^+ ions undergo fast stochastic hopping across a shallow potential energy landscape, which is facilitated by the dynamics of the crystalline framework. Specific phonon modes of the soft crystalline lattice enable an order-of-magnitude enhancement in Li^+ ion diffusivity at ambient temperature, through the dynamic breathing of hopping bottlenecks. Therefore, this suggests tailoring the dynamics of the host framework to optimize ionic conductivity of solid-state electrolytes.

ACKNOWLEDGEMENTS

Neutron scattering data collection, MD simulations and analysis by JD, simulations by H-ML, as well as manuscript writing (JD, OD), were supported by a U.S. National Science Foundation DMREF project under award DMR-2119273. Initial analysis and simulations by MKG were supported by DOE award DE-SC0019978. Sample synthesis by CR and WGZ was supported by the Deutsche Forschungsgemeinschaft under grant number ZE 1010/4-1. The use of Oak Ridge National Laboratory's Spallation Neutron Source was sponsored by the Scientific User Facilities Division, Office of Basic Energy Sciences, U.S. DOE. Theoretical calculations were performed using the National Energy Research Scientific Computing Center, a U.S. DOE Office of Science User Facility supported by the Office of Science of the U.S. DOE under Contract No. DE-AC02-05CH11231.

AUTHOR CONTRIBUTIONS

OD and JD designed the research. JD, MKG, NCO, and DLA performed neutron scattering measurements. CR and WGZ grew and characterized the samples. JD, MKG, and H-ML performed simulations and analyzed data. JD and OD wrote the paper.

COMPETING INTERESTS

The authors declare no competing interests.

TABLES

	BASIS	MLMD narrow	MLMD wide
d_{jump} (Å)	2.4±0.4	2.7±0.1	1.2±0.1
τ (ps)	19.2±2.4	18.6±0.6	1.2±0.2
D (x10^{-6} cm^2/s)	5.0±2.1	6.6±0.7	20.5±8.2

TABLE I. Hopping distances, residence time and diffusion coefficients at 600 K of QENS spectra from BASIS and MLMD, both from Chudley-Elliot analysis. MLMD narrow and wide represents slow inter-cage and fast intra-cage/doublet processes, respectively.

FIGURE LEGENDS/CAPTIONS

FIG. 1. (color) **Quadratic to linear vibrational spectrum reveals non-Debye dynamics in solid electrolyte.** (a) Crystal structure of Li_6PS_5Cl. Li, P, S, and Cl atoms are shown in green-white, purple, yellow, and brown, respectively. Cl^- form a face-centered cubic lattice (Wyckoff 4*a*) with PS_4^{3-} units in the octahedral sites centered at P^{5+} (Wyckoff 4*b*), and surrounded by S^{2-} in the Wyckoff 16*e* sites. The remaining S^{2-} ("free S") occupy half of the tetrahedral sites (Wyckoff 4*c*). Li^+ occupy the Wyckoff 48*h* sites surrounding the 4*c* S^{2-} with 50% occupancy. (b) Probability distribution of Li^+ at 600 K with isosurfaces value 2×10^{-11} Bohr^{-3} computed from MLMD. Arrows in (a) show three conventional types of Li^+ hops reported in the literature, Li^+ probability in (b) shows that diffusion occurs through intermediate sites (see text). (c) $S(E)$ at $E_i = 25$ measured at ARCS at 100, 200, 300, 400, 500, 600, and 680 K. (d) Corresponding vibrational spectra. The dashed lines are the replica of the 100 K data with the same offset as references. The shoulder around 8 meV and the peak at 15 meV broaden with increasing temperature as a result of the enhanced phonon-phonon scattering. Strong softening is observed. (e) Low-E spectrum from INS (top) and MLMD (bottom). A finite spectral weight at $\omega \to 0$ is observed in both INS and MLMD at 600 K from Li^+ diffusion. The $g(\omega \to 0)$ estimated from the hopping coefficient in QENS is plotted as purple cross. Shaded regions represent the difference between the two INS spectra or the calculated Li partial DOS from MLMD. (f) Linear and quadratic fit of low-E INS spectrum. At 200 K, spectral intensity increases quadratically with energy. At 600 K, clear excess spectral intensity (no vertical offset) and linear frequency dependence are observed, strongly deviating from Debye model. The INS data below 1.5 meV are removed (elastic scattering from ARCS resolution). The error bars represent one standard deviation which include statistical uncertainties of the neutron flux.

FIG. 2. (color) **Ionic diffusion from back-scattering spectroscopy and MLMD.** (a) Temperature dependent QENS spectra of $^7Li_6PS_5Cl$, measured at $Q = 1.5\pm0.1$ Å^{-1} at 100, 300, 400, 500, 600, and 680 K, offset vertically. Upon heating above 300 K, clear broadening is observed, as a characteristic of decaying correlation from ionic diffusion. Factors of 2, 3 and 4 are applied for 500, 600, and 680 K, respectively, to help visualizing the broadening. (b) The QENS fit at 600 K, with raw data (grey), and the total fit (orange). QENS spectra are fitted with a delta function (blue), a lorentzian (red), and a linear background (black), convoluted with the instrument resolution (30 K measurements). MLMD calculated spectrum for slow inter-cage diffusion is shown in green. (c) Chudley-Elliot fits at 600 K from BASIS (blue) and MLMD (orange). Γ is the HWHM. (d) Arrhenius plot of the diffusion coefficients. An activation energy of 0.11 and 0.16 eV are estimated from QENS and MLMD, respectively. The error bars represent one standard deviation which include statistical uncertainties of the neutron flux.

FIG. 3. (color) **Effect of lattice flexibility on ionic diffusion and selective breakdown of phonon quasiparticles.** (a) Selected sub-trajectory (500 ps) at 600 K for unconstrained MLMD showing a Li^+ exploring multiple cages. The green trajectory is that of a single Li^+ ion across multiple cages. (b) Li^+ trajectory (500 ps) at 600 K for fixed host case. Long-range diffusion is inhibited by the rigid structural bottleneck. Red segments highlight 0.2 ps portions of the trajectories corresponding to inter-cage hops. Back-and-forth jumps within 1 ps are removed. Black box indicates the unit-cell. (c) Li PDOS for several MLMD constraints. Higher intensity and zero-limit value is observed for unconstrained case (higher diffusion coefficient) in contrast with the fixed PS_4^{3-} and fixed host cases. Inset shows the time-averaged area distributions of the structrual bottleneck between adjacent T2-T2 sites. (d) MLMD calculated $\chi''(\mathbf{Q},\omega)$ for longitudinal modes along [0,0,L] at 600 K. 1D spectral functions for (e) longitudinal acoustic phonons at $\mathbf{Q}$=0,0,0.5 (r.l.u.) and (f) Transverse acoustic phonons at $\mathbf{Q}$=0,1.5,4 (r.l.u.). At 600 K, longitudinal acoustic phonons become very broad and the breakdown of short wavelength transverse acoustic phonons is observed due to the disruption of long-range periodicity from the diffusion Li^+.

REFERENCES

[1] Gerald D Mahan and Walter L Roth, editors. Superionic Conductors. Springer US, Boston, MA, 1976.

[2] J. B. Boyce and B. A. Huberman. Superionic conductors: Transitions, structures, dynamics. Physics Reports, 51:189–265, 1979.

[3] M. Parrinello, A. Rahman, and P. Vashishta. Structural transitions in superionic conductors. Phys. Rev. Lett., 50:1073–1076, Apr 1983.

[4] Paul M Chaikin, Tom C Lubensky, and Thomas A Witten. Principles of condensed matter physics, volume 10. Cambridge university press Cambridge, 1995.

[5] Göran Grimvall. Thermophysical properties of materials. Elsevier, 1999.

[6] Peter Brüesch. Phonons: Theory and experiments I: Lattice dynamics and Models of interatomic forces, volume 34. Springer Science & Business Media, 2012.

[7] Norman Henry March and Mario P Tosi. Atomic dynamics in liquids. Courier Corporation, 1991.

[8] Richard M Stratt. The instantaneous normal modes of liquids. Accounts of Chemical Research, 28(5):201–207, 1995.

[9] T Keyes. Instantaneous normal mode approach to liquid state dynamics. The Journal of Physical Chemistry A, 101(16):2921–2930, 1997.

[10] Alessio Zaccone and Matteo Baggioli. Universal law for the vibrational density of states of liquids. Proceedings of the National Academy of Sciences, 118(5):e2022303118, 2021.

[11] Hideyuki Mizuno, Hayato Shiba, and Atsushi Ikeda. Continuum limit of the vibrational properties of amorphous solids. Proceedings of the National Academy of Sciences, 114(46):E9767–E9774, 2017.

[12] Jennifer L Niedziela, Dipanshu Bansal, Andrew F May, Jingxuan Ding, Tyson Lanigan-Atkins, Georg Ehlers, Douglas L Abernathy, Ayman Said, and Olivier Delaire. Selective breakdown of phonon quasiparticles across superionic transition in $CuCrSe_2$. Nature Physics, 15(1):73, 2019.

[13] Jingxuan Ding, Jennifer L Niedziela, Dipanshu Bansal, Jiuling Wang, Xing He, Andrew F May, Georg Ehlers, Douglas L Abernathy, Ayman Said, Ahmet Alatas, et al. Anharmonic lattice dynamics and superionic transition in agcrse2. Proceedings of the National Academy of Sciences, 117(8):3930–3937, 2020.

[14] L Xie, JH Feng, R Li, and JQ He. First-principles study of anharmonic lattice dynamics in low thermal conductivity agcrse 2: Evidence for a large resonant four-phonon scattering. Physical Review Letters, 125(24):245901, 2020.

[15] Chen Wang and Yue Chen. Highly selective phonon diffusive scattering in superionic layered $AgCrSe_2$. npj Computational Materials, 6(1):1–6, 2020.

[16] Mayanak K Gupta, Jingxuan Ding, Dipanshu Bansal, Douglas L Abernathy, Georg Ehlers, Naresh C Osti, Wolfgang G Zeier, and Olivier Delaire. Strongly anharmonic phonons and their role in superionic diffusion and ultralow thermal conductivity of cu7pse6. Advanced Energy Materials, page 2200596, 2022.

[17] Gabriel Krenzer, Chang-Eun Kim, Kasper Tolborg, Benjamin J Morgan, and Aron Walsh. Anharmonic lattice dynamics of superionic lithium nitride. Journal of Materials Chemistry A, 10(5):2295–2304, 2022.

[18] Kunio Wakamura. Roles of phonon amplitude and low-energy optical phonons on superionic conduction. Physical Review B, 56(18):11593, 1997.

[19] Matthias T Agne, Joop Frerichs, Shuo Wang, Georg Dewald, Tim Bernges, Nella Vargas-Barbosa, Yifei Mo, Michael Hansen, and Wolfgang Zeier. Relating critical phonon occupation to activation barrier in fast lithium-ion conductors. 2022.

[20] Marvin A Kraft, Sean P Culver, Mario Calderon, Felix Böcher, Thorben Krafuskopf, Anatoliy Senyshyn, Christian Dietrich, Alexandra Zevalkink, Jürgen Janek, and Wolfgang G Zeier. Influence of lattice polarizability on the ionic conductivity in the lithium superionic argyrodites li6ps5x (x= cl, br, i). Journal of the American Chemical Society, 139(31):10909–10918, 2017.

[21] Thorben Krauskopf, Sokseiha Muy, Sean P Culver, Saneyuki Ohno, Olivier Delaire, Yang Shao-Horn, and Wolfgang G Zeier. Comparing the descriptors for investigating the influence of lattice dynamics on ionic transport using the superionic conductor na3ps4–xsex. Journal of the American Chemical Society, 140(43):14464–14473, 2018.

[22] Sokseiha Muy, John C Bachman, Livia Giordano, Hao-Hsun Chang, Douglas L Abernathy, Dipanshu Bansal, Olivier Delaire, Satoshi Hori, Ryoji Kanno, Filippo Maglia, et al. Tuning mobility and stability of lithium ion conductors based on lattice dynamics. Energy and Environmental Science, 11(4):850–859, 2018.

[23] Sokseiha Muy, Johannes Voss, Roman Schlem, Raimund Koerver, Stefan J Sedlmaier, Filippo Maglia, Peter Lamp, Wolfgang G Zeier, and Yang Shao-Horn. High-throughput screening of solid-state li-ion conductors using lattice-dynamics descriptors. Iscience, 16:270–282, 2019.

[24] Cibrán López, Agustí Emperador, Edgardo Saucedo, Riccardo Rurali, and Claudio Cazorla. Universal ion-transport descriptors and classes of inorganic solid-state electrolytes. Materials horizons, 10(5):1757–1768, 2023.

[25] Dominique Larcher and Jean-Marie Tarascon. Towards greener and more sustainable batteries for electrical energy storage. Nature chemistry, 7(1):19–29, 2015.

[26] John B Goodenough and Kyu-Sung Park. The li-ion rechargeable battery: a perspective. Journal of the American Chemical Society, 135(4):1167–1176, 2013.

[27] Jürgen Janek and Wolfgang G Zeier. A solid future for battery development. Nature Energy, 1(9):1–4, 2016.

[28] Theodosios Famprikis, Pieremanuele Canepa, James A Dawson, M Saiful Islam, and Christian Masquelier. Fundamentals of inorganic solid-state electrolytes for batteries. Nature materials, 18(12):1278–1291, 2019.

[29] Noriaki Kamaya, Kenji Homma, Yuichiro Yamakawa, Masaaki Hirayama, Ryoji Kanno, Masao Yonemura, Takashi Kamiyama, Yuki Kato, Shigenori Hama, Koji Kawamoto, et al. A lithium superionic conductor. Nature materials, 10(9):682, 2011.

[30] Yuki Kato, Satoshi Hori, Toshiya Saito, Kota Suzuki, Masaaki Hirayama, Akio Mitsui, Masao Yonemura, Hideki Iba, and Ryoji Kanno. High-power all-solid-state batteries using sulfide superionic conductors. Nature Energy, 1(4):1–7, 2016.

[31] Parvin Adeli, J David Bazak, Kern Ho Park, Ivan Kochetkov, Ashfia Huq, Gillian R Goward, and Linda F Nazar. Boosting solid-state diffusivity and conductivity in lithium superionic argyrodites by halide substitution. Angewandte Chemie, 131(26):8773–8778, 2019.

[32] Hans-Jörg Deiseroth, Shiao-Tong Kong, Hellmut Eckert, Julia Vannahme, Christof Reiner, Torsten Zaiß, and Marc Schlosser. Li6ps5x: a class of crystalline li-rich solids with an unusually high li+ mobility. Angewandte Chemie International Edition, 47(4):755–758, 2008.

[33] P Brüesch, L Pietronero, S Strässler, and HR Zeller. Brownian motion in a polarizable lattice: Application to superionic conductors. Physical Review B, 15(10):4631, 1977.

[34] Qing Zhang, Daxian Cao, Yi Ma, Avi Natan, Peter Aurora, and Hongli Zhu. Sulfide-based solid-state electrolytes: synthesis, stability, and potential for all-solid-state batteries. Advanced Materials, 31(44):1901131, 2019.

[35] Roman Schlem, Michael Ghidiu, Sean P Culver, Anna-Lena Hansen, and Wolfgang G Zeier. Changing the static and dynamic lattice effects for the improvement of the ionic transport properties within the argyrodite li6ps5–x se x i. ACS Applied Energy Materials, 3(1):9–18, 2019.

[36] I Hanghofer, M Brinek, SL Eisbacher, B Bitschnau, M Volck, V Hennige, I Hanzu, D Rettenwander, and HMR Wilkening. Substitutional disorder: structure and ion dynamics of the argyrodites li6ps5cl, li6ps5br and li6ps5i. Physical Chemistry Chemical Physics, 21(16):8489–8507, 2019.

[37] Ulrich Köhler and Christian Herzig. On the correlation between self-diffusion and the low-frequency la –<111> phonon mode in bcc metals. Philosophical Magazine A, 58(5):769–786, 1988.

[38] Caleb Stamper, David Cortie, Zengji Yue, Xiaolin Wang, and Dehong Yu. Experimental confirmation of the universal law for the vibrational density of states of liquids. The Journal of Physical Chemistry Letters, 13(13):3105–3111, 2022.

[39] Mayanak K Gupta, Jingxuan Ding, Naresh C Osti, Douglas L Abernathy, William Arnold, Hui Wang, Zachary Hood, and Olivier Delaire. Fast na diffusion and anharmonic phonon dynamics in superionic na 3 ps 4. Energy & Environmental Science, 14(12):6554–6563, 2021.

[40] Martin T Dove. Introduction to lattice dynamics. Number 4. Cambridge university press, 1993.

[41] Peter Brüesch. Phonons: Theory and Experiments I, volume 34 of Springer Series in Solid-State Sciences. Springer Berlin Heidelberg, Berlin, Heidelberg, 1982.

[42] K Funke. Jump relaxation in solid electrolytes. Progress in Solid State Chemistry, 22(2):111–195, 1993.

[43] Andrew K Jonscher. Dielectric relaxation in solids. Journal of Physics D: Applied Physics, 32(14):R57, 1999.

[44] Junko Habasaki, Carlos Leon, and KL Ngai. Dynamics of glassy, crystalline and liquid ionic conductors. Top Appl Phys, 132:355–410, 2017.

[45] Nicolo Minafra, Marvin A Kraft, Tim Bernges, Cheng Li, Roman Schlem, Benjamin J Morgan, and Wolfgang G Zeier. Local charge inhomogeneity and lithium distribution in the superionic argyrodites li6ps5x (x= cl, br, i). Inorganic Chemistry, 59(15):11009–11019, 2020.

[46] Niek JJ De Klerk, Irek Rosło, and Marnix Wagemaker. Diffusion mechanism of li argyrodite solid electrolytes for li-ion batteries and prediction of optimized halogen doping: the effect of li vacancies, halogens, and halogen disorder. Chemistry of Materials, 28(21):7955–7963, 2016.

[47] Benjamin J Morgan. Mechanistic origin of superionic lithium diffusion in anion-disordered li6ps5 x argyrodites. Chemistry of Materials, 33(6):2004–2018, 2021.

[48] Shiao-Tong Kong, Hans-Jörg Deiseroth, Christof Reiner, Özgül Gün, Elmar Neumann, Clemens Ritter, and Dirk Zahn. Lithium argyrodites with phosphorus and arsenic: order and disorder of lithium atoms, crystal chemistry, and phase transitions. Chemistry–A European Journal, 16(7):2198–2206, 2010.

[49] Enyue Zhao, Lunhua He, Zhigang Zhang, Jean-Marie Doux, Darren HS Tan, Erik A Wu, Grayson Deysher, Yu-Ting Chen, Jinkui Zhao, Fangwei Wang, et al. New insights into li distribution in the superionic argyrodite li 6 ps 5 cl. Chemical Communications, 57(82):10787–10790, 2021.

[50] Tasso Springer. Quasielastic neutron scattering for the investigation of diffusive motions in solids and liquids. Springer Tracts in Modern Physics, Volume 64, pages 1–100, 1972.

[51] Xuyong Feng, Po-Hsiu Chien, Yan Wang, Sawankumar Patel, Pengbo Wang, Haoyu Liu, Marcello Immediato-Scuotto, and Yan-Yan Hu. Enhanced ion conduction by enforcing structural disorder in li-deficient argyrodites li6- xps5- xcl1+ x. Energy Storage Materials, 30:67–73, 2020.

[52] Zhenming Xu, Xi Chen, Hong Zhu, and Xin Li. Anharmonic cation-anion coupling dynamics assisted lithium-ion diffusion in sulfide solid electrolytes. Advanced Materials, page 2207411, 2022.

[53] Mayanak Kumar Gupta, Sajan Kumar, Ranjan Mittal, and Samrath L Chaplot. Soft-phonon anharmonicity, floppy modes, and na diffusion in na 3 f y (y= s, se, te): Ab initio and machine-learned molecular dynamics simulations. Physical Review B, 106(1):014311, 2022.

[54] Jeffrey G Smith and Donald J Siegel. Ion migration mechanisms in the sodium sulfide solid electrolyte na3–x sb1–x w x s4. Chemistry of Materials, 34(9):4166–4171, 2022.

[55] Douglas R MacFarlane and Maria Forsyth. Plastic crystal electrolyte materials: new perspectives on solid state ionics. Advanced materials, 13(12-13):957–966, 2001.

[56] Zhizhen Zhang and Linda F Nazar. Exploiting the paddle-wheel mechanism for the design of fast ion conductors. Nature Reviews Materials, pages 1–17, 2022.

[57] Hong Fang and Puru Jena. Argyrodite-type advanced lithium conductors and transport mechanisms beyond peddle-wheel effect. Nature communications, 13(1):1–11, 2022.

[58] KyuJung Jun, Byungju Lee, Ronald L. Kam, and Gerbrand Ceder. The nonexistence of a paddlewheel effect in superionic conductors. Proceedings of the National Academy of Sciences, 121(18):e2316493121, 2024.

METHODS

Sample Preparation: We synthesis $^{7}Li_6PS_5Cl$ to minimize the strong neutron absorption of ^{6}Li. Stoichiometric amounts of $^{7}LiCl$ (99 atom% ^{7}Li, Sigma-Aldrich), $^{7}Li_2S$ ($\geq$99 atom% ^{7}Li, Sigma-Aldrich) and P_2S_5 (Sigma-Aldrich) were hand ground in an agate mortar for 15 minutes. The ground powder was pressed into pellets and sealed into carbon coated quartz ampoules, the quartz ampoules were preheated under dynamic vacuum at 800 °C for 2 hours. The solid-state reaction took place in a Nabertherm furnace for 2 weeks at 550 °C with a heating ramp of 100 °C/h and cooled naturally. The obtained product was hand ground and sealed under vacuum (4.2×10^{-1} mbar) in a 10 mm quartz ampoule for the measurement of the neutron diffraction data. Diffraction patterns from a StadiP X-Ray diffractometer from STOE in Debye-Scherrer geometry with a

Cu-Kα radiation (λ1=1.545 Å) were compared with the theoretical diffraction pattern generated using the CrystalDiffract diffraction software (CrystalMaker Software Ltd, Oxford, England, www.crystalmaker.com). The relative intensity and peak positions are in very good agreement.

Quasielastic Neutron Scattering: The QENS measurements were performed using the BASIS backscattering spectrometer at the Spallation Neutron Source, Oak Ridge National Laboratory [1]. 6 grams of $^7Li_6PS_5Cl$ were flame sealed in two fused-silica ampoules. The ampoules were aligned and wrapped together with aluminum foil to approximate a flat plate geometry. Another two empty ampoules with identical configurations are used to collect empty can signal. Si(111) analyzers was used with neutron wavelength 6.4 Å and chopper frequency of 60 Hz. This configuration yields an energy bandwidth of $-100 < E < 100\,\mu$eV with energy resolution 3.5 μeV, and a momentum transfer coverage of $0.2 < Q < 2.0\,\text{Å}^{-1}$. Samples are mounted in a thin wall aluminum can in a top-loading closed-cycle refrigerator. We measured $T = 30$, 100, 200, 300, 400, 450, 500, 550, 600, and 680 K. The 30 K data shows no broadening, which is used as a sample dependent resolution function. The collected data from the area detectors were transformed from instrument coordinates to physical coordinates $\mathbf{Q}$, E, using algorithms implemented in Mantid analysis software [2]. All data were normalized and corrected by a standard vanadium sample. The data were grouped into Q bins of width $0.2\,\text{Å}^{-1}$ with center ranging from 0.3 to $1.9\,\text{Å}^{-1}$. The suppression of the QENS peak height arises because the elastic intensity decreases upon heating due to the large Debye-Waller factor of the mobile Li^+ sublattice. The reversibility is checked after cooling back to 300 K and gives the same spectra as the one before heating, which confirms that the sample remain intact after heating to 680 K.

The model scattering function we used to fit the QENS data can be written as:

$$I(Q,\omega) = \left[A\delta(\omega-\omega_0) + B\frac{1}{\pi}\frac{\Gamma(Q)}{\Gamma^2(Q)+(\omega-\omega_0)^2}\right] \otimes R(Q,\omega) + BG(Q) \quad (6)$$

where the scattering intensity $I(Q,\omega)$ is fitted with an elastic line (δ function), a quasielastic peak (Lorentzian function) convoluted with the sample depenedent instrument resolution function $R(Q,\omega)$, and a linear background $BG(Q)$. A, B are constants.

The polycrystalline samples need to be hold in a container, e.g., an ampoule or a standard aluminum can. A measurement of the empty container at the identical condition is required to extract the true signal from the sample:

$$I_{sample} = I_{raw} - \xi \cdot I_{emptycan} \quad (7)$$

where ξ is the self-shielding factor, normally < 1. This factor is applied because the scattering condition will change when sample is placed in the container. The value of ξ can be determined by checking the residue of the diffraction pattern from the sample holder after the subtraction.

The fitted half-width at half-maximum Γ (HWHM) at each temperature is fitted with a jump-like diffusion Chudley-Elliot (CE) model [3]:

$$\Gamma(Q,\omega) = \frac{1}{\tau}\left(1 - \frac{sin(Qd)}{Qd}\right) \quad (8)$$

where d and τ are the average jump-length and the residence time. At the low-Q limit, the variance of $\Gamma(Q)$ can be used to extract the coefficient:

$$D = d^2/6\tau \quad (9)$$

Although the $^7Li_6PS_5Cl$ are found to be less air sensitive compared to other LISICONs, the moisture can cause its decomposition. Thus, the samples were sealed in preheated quartz ampoules under vacuum as written in the synthesis section. Additional aluminum foil and sample can is used to properly mount the sample to the instrument, as shown in Fig. **??**. This unconventional setting adapted in this experiment results in a complex scattering environment compared to conventional flat cell geometry. The elastic peak intensity is used to evaluate a proper empty can factor ξ (Equ. 7). In this case, we assume the raw signal has extra scattering of the empty can compared to the intrinsic sample signal. As can be seen in Fig. **??**, $\xi = 1$ results in a negative subtraction, meaning the empty can has more scattering compared to the case with $^7Li_6PS_5Cl$. The extra scattering could originate from the absorption from Cl^-, and due to uneven setting between the sample and empty can. Nevertheless, a correction factor of $\xi = 0.75$ shows proper correction in the following analysis process as we will show later.

Inelastic Neutron Scattering: INS measurements were performed with the same powder samples as BASIS using ARCS [4]. In the ARCS measurements, we used a top-loading closed-cycle refrigerator with a hot stage. Incident energy $E_i = 180$ meV was used to cover the whole phonon energy range and $E_i = 25$ and 50 meV render finer resolution to capture the details of the low-energy phonon modes. Data were collected at the same temperature as BASIS from 100 to 680 K. The Fermi chopper and the t-zero chopper were on automatic modes. These configurations provided an estimated elastic line energy resolution of 0.96 meV at $E_i = 25$ meV, 1.80 meV at $E_i = 50$ meV and 10.14 meV at $E_i = 180$ meV. An oscillating radial collimator was used, and the empty can background scattering data were collected with an identical configuration as sample measurement. $S(E)$ is summed over the whole Q-range. The analysis of phonon density of state (DOS) was performed within the incoherent scattering approximation. Corrections for multiphonon and multiscattering were applied as detailed in Ref. 5. The elastic peak region ($E < 1.5$ meV) for $E_i = 25$ meV was removed. No

extrapolation was included due to the non-Debye dynamics from superionic Li^+ diffusion. The neutron-weighted DOS is expressed as:

$$\begin{aligned} g(\omega) &= \sum_i f_i \frac{\sigma_i}{m_i} g_i(\omega) \\ g_i(\omega) &= \sum_{j,\mathbf{q}} |e_i(j,\mathbf{q})|^2 \delta(\omega - \omega(j,(q))) \end{aligned} \tag{10}$$

where f_i, σ_i, m_i and $g_i(\omega)$, $e_i(j,\mathbf{q})$, $\omega(j,\mathbf{q})$ are the atomic fraction, neutron total cross-section, atomic mass, partial density of states, phonon eigenvectors and phonon frequencies of atom i. We weighted the simulated DOS with the neutron cross-sections so that it can be directly compared with the experimentally measured DOS.

DFT, AIMD, and MLMD simulations: Theoretical calculations were performed with the Vienna *Ab initio* Simulation Package (VASP 5.4) [6–8], using the PBE exchange-correlation functional [9, 10]. The cubic unit cell consists of 52 atoms with a lattice constant of 9.859 Å. 24 Li^+ are removed randomly to ensure the stoichiometry of the 50% occupancy. 50% disorder of Cl^-/S^{2-} is also randomly generated. A 2×2×2 k-point mesh with a plane-wave cut-off energy of 500 eV was used. The electronic self-consistent loop convergence was set to 10^{-6} eV.

Ab initio molecular dynamics (AIMD) simulations were performed using NVT-ensemble with Nosé–Hoover thermostat from 100 to 800 K with 100 K steps. Each simulation trajectories were 2 ps long with a time step of 2 fs to sample the potential energy surface. Longer trajectories at 200 and 600 K of 20 ps with 2×2×1 were calculated to validate against MLMD trajectories.

We used DeePMD-kit code [11] to train a surrogate neural-network force-field based on machine learning. The surrogate force-field was validated against reference AIMD data, including out-of-distribution tests with larger cell size than the training data (Fig. **??**). Dynamic properties were also benchmarked against AIMD (Fig. **??**-**??**).

MLMD simulations were performed with LAMMPS [12] on 3×3×3 supercell (1404 atoms) with NVT and NPT ensembles. Calculations were done with both the experimental lattice parameters and NPT relaxed lattice parameters at specific temperature. Temperature and pressure were controlled by Nosé-Hoover thermostat and barostat with time constant 0.1 ps and 1 ps. For QENS calculation, the trajectory is $\sim$ 1 ns long which gives an energy resolution of 3.2 μeV, and momentum resolution $\sim$ 0.2 $Å^{-1}$. Constraint calculation were performed on 2×2×2 supercell (416 atoms). Unconstraint case at two supercells were tested first which yields the same MSD. Five constraint cases are considered in MLMD: (i) making PS_4^{3-} units rigid bodies (green diamonds) that can rotate or translate as a whole; (ii) rigid PS_4^{3-} units with frozen rotations (brown triangles), only allowing translational vibrations ("wiggling"); (iii) fixing S and P ions in PS_4^{3-} units to their initial positions (blue pentagons), while free S, Cl and Li ions are mobile; (iv) fixing positions of all free S and Cl ions (pink hexagons); (v) fixing all framework ions (P, S, Cl), with only Li^+ mobile (black crosses). For $S(\mathbf{Q},\omega)$ calculations of low energy phonons, we used 2×2×20 supercell (4160 atoms) for the longitudinal mode along 00L, which give commensurate $\mathbf{Q}$ of 0.1 in reciprocal lattice unit (r.l.u.) along the 00L direction. For TA phonons along 0H0, we used 2×10×10 supercell (10400 atoms), which give commensurate $\mathbf{Q}$ of 0.2 r.l.u., in all directions. Three parallel trajectories are averaged to improve the statistics of the data.

The mean square displacement (MSD), is calculated to extract the diffusion coefficient from MLMD:

$$< u_i^2(t) >= \frac{1}{N} \sum_{i=1}^{N_i} \langle |r_i(t) - r_i(0)|^2 \rangle \tag{11}$$

where N_i is the number of atoms, $r_i(t)$ is the position of the ith atom at time t. <> represents the ensemble average. The self-diffusion coefficient is estimated using Einstein relation over a period τ:

$$D_i(T) = \frac{< u_i^2(\tau) >}{6\tau} \tag{12}$$

The total neutron scattering intensity is the sum of the coherent and incoherent components [13]:

$$I(Q,\omega) \propto \sum_{i,j} b_{coh}^i b_{coh}^j S_{coh}^{ij}(Q,\omega) + \sum_j b_{inc}^{j^2} S_{inc}^j(Q,\omega) \tag{13}$$

where b_{coh}^i and b_{inc}^i are the coherent and incoherent scattering length of the i^{th} atoms. For Li, $\sigma_{coh}^{7Li} (= 4\pi b_{coh}^2) =$ 0.619 barn and $\sigma_{inc}^{7Li} (= 4\pi b_{inc}^2) =$ 0.78 barn, thus, both contributions should be considered. The coherent scattering measures the space-time correlations between a pair of atoms, which probes a correlated diffusion process. The incoherent scattering measures the time correlation of the positions of a single atom (self-diffusion) [14, 15]. As can be seen in Fig. **??**, the incoherent scattering of Li^+ dominates the QENS signal whose width increases with Q, matching the observations in our neutron measurements, whereas the coherent scattering has almost negligible contribution to the QENS broadening and remain constant above 5 μeV (except for phonon excitation at meV energies). This establishes that the Li^+ self-diffusion generates the QENS signal. Concerted motions of multiple ions such as lithium cage rearrangements are possible, as simulated in Ref. [16], which would show up in the (weak) coherent scattering signal. The simulated $S_{inc}^{Li}(Q,\omega)$ is fitted with two Lorentzians to distinguish the different timescales for inter-cage and intra-cage/doublet hops (elastic line excluded).

DATA AND CODE AVAILABILITY

All data that support the conclusion of this work are available from the corresponding author upon reasonable request. The numerical data for the figures

are available from the Harvard Dataverse Repository at https://doi.org/10.7910/DVN/RCBK4U. The codes that support findings of the study are available from the corresponding author upon reasonable request.

METHODS-ONLY REFERENCES

[1] Eugene Mamontov and Kenneth W Herwig. A time-of-flight backscattering spectrometer at the spallation neutron source, basis. Review of Scientific Instruments, 82(8):085109, 2011.

[2] O Arnold, J C Bilheux, J M Borreguero, A Buts, S I Campbell, L Chapon, M Doucet, N Draper, R Ferraz Leal, M A Gigg, V E Lynch, A Markvardsen, D J Mikkelson, R L Mikkelson, R Miller, K Palmen, P Parker, G Passos, T G Perring, P F Peterson, S Ren, M A Reuter, A T Savici, J W Taylor, R J Taylor, R Tolchenov, W Zhou, and J Zikovsky. Mantid—Data analysis and visualization package for neutron scattering and μSR experiments. Nuclear Instruments and Methods in Physics Research Section A: Accelerators, Spectrometers, Detectors and Associated Equipment, 764:156–166, November 2014.

[3] CT Chudley and RJ Elliott. Neutron scattering from a liquid on a jump diffusion model. Proceedings of the Physical Society (1958-1967), 77(2):353, 1961.

[4] D L Abernathy, M B Stone, M J Loguillo, M S Lucas, O Delaire, X Tang, J Y Y Lin, and B Fultz. Design and operation of the wide angular-range chopper spectrometer ARCS at the Spallation Neutron Source. Review of Scientific Instruments, 83(1):015114, 2012.

[5] YY Lin, Fahima Islam, and Max Kresh. Multiphonon: Phonon density of states tools for inelastic neutron scattering powder data. Journal of Open Source Software, 3(21), 2018.

[6] G Kresse and J Hafner. Ab initio molecular dynamics for liquid metals. Physical Review B, 47(1):558–561, January 1993.

[7] G Kresse and J Furthmüller. Efficient iterative schemes for ab initio total-energy calculations using a plane-wave basis set. Physical Review B, 54(16):11169–11186, October 1996.

[8] G Kresse and J Furthmüller. Efficiency of ab initio total energy calculations for metals and semiconductors using a plane-wave basis set. Computational Materials Science, 6(1):15–50, July 1996.

[9] J.P. Perdew and A. Zunger. Self-interaction correction to density-functional approximations for many-electron systems. Physical Review B, 23:5048–5079, 1981.

[10] J.P. Perdew, K. Burke, and M. Ernzerhof. Generalized gradient approximation made simple. Physical Review Letters, 77:3865–3868, 1996.

[11] Han Wang, Linfeng Zhang, Jiequn Han, and E Weinan. Deepmd-kit: A deep learning package for many-body potential energy representation and molecular dynamics. Computer Physics Communications, 228:178–184, 2018.

[12] A. P. Thompson, H. M. Aktulga, R. Berger, D. S. Bolintineanu, W. M. Brown, P. S. Crozier, P. J. in 't Veld, A. Kohlmeyer, S. G. Moore, T. D. Nguyen, R. Shan, M. J. Stevens, J. Tranchida, C. Trott, and S. J. Plimpton. LAMMPS - a flexible simulation tool for particle-based materials modeling at the atomic, meso, and continuum scales. Comp. Phys. Comm., 271:108171, 2022.

[13] Mayanak K Gupta, Jingxuan Ding, Naresh C Osti, Douglas L Abernathy, William Arnold, Hui Wang, Zachary Hood, and Olivier Delaire. Fast na diffusion and anharmonic phonon dynamics in superionic na 3 ps 4. Energy & Environmental Science, 14(12):6554–6563, 2021.

[14] Stephen W Lovesey. Theory of neutron scattering from condensed matter. 1984.

[15] Tasso Springer. Quasielastic neutron scattering for the investigation of diffusive motions in solids and liquids. Springer Tracts in Modern Physics, Volume 64, pages 1–100, 2006.

[16] Benjamin J Morgan. Mechanistic origin of superionic lithium diffusion in anion-disordered li6ps5 x argyrodites. Chemistry of Materials, 33(6):2004–2018, 2021.

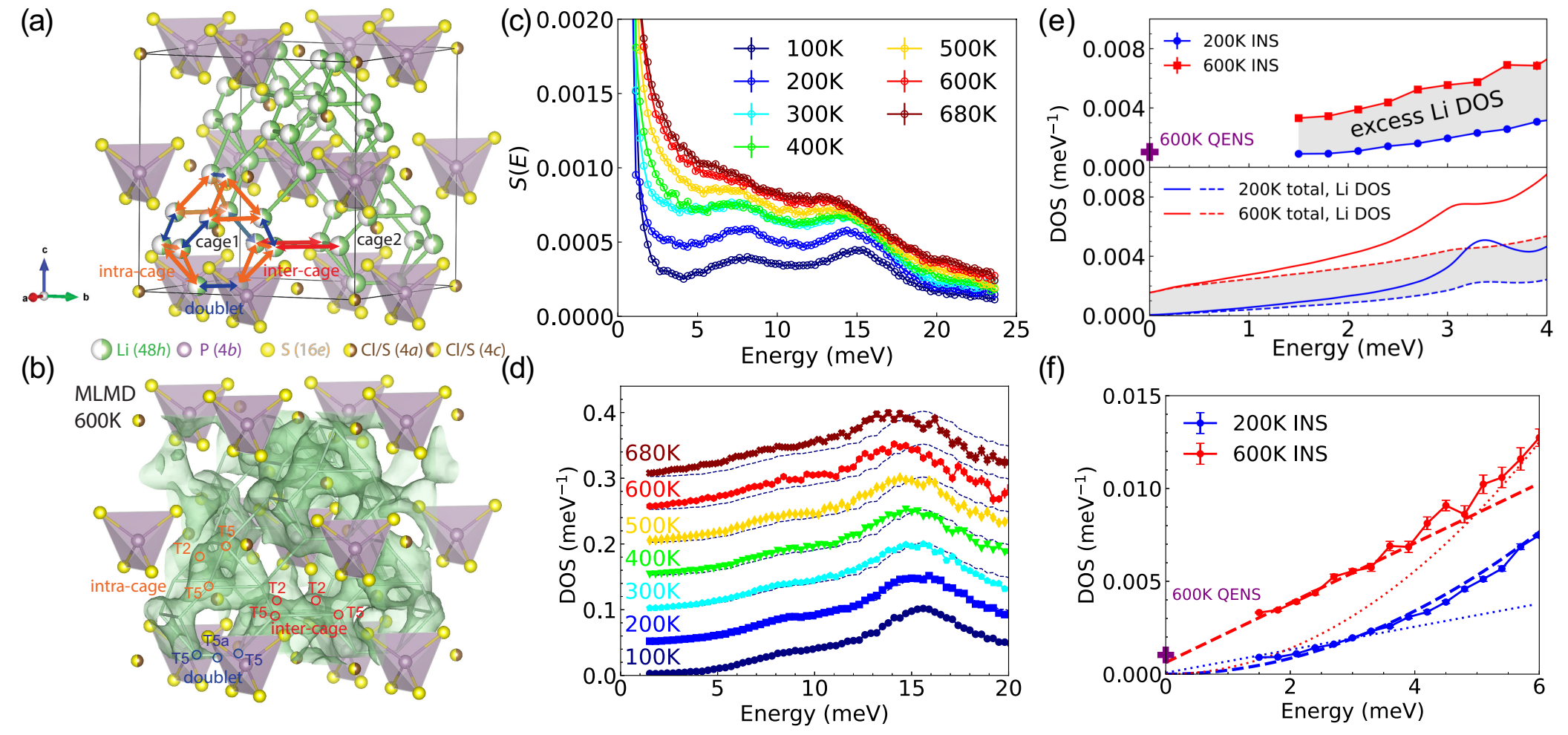
(a)
cage1
cage2
intra-cage
inter-cage
doublet
c
a
b
Li (48h) P (4b) S (16e) Cl/S (4a) Cl/S (4c)
(b)
MLMD
600K
T2
T5
T5a
intra-cage
inter-cage
doublet
(c)
S(E)
100K
200K
300K
400K
500K
600K
680K
Energy (meV)
(d)
DOS (meV^{-1})
680K
600K
500K
400K
300K
200K
100K
Energy (meV)
(e)
200K INS
600K INS
600K QENS
excess Li DOS
200K total, Li DOS
600K total, Li DOS
DOS (meV^{-1})
Energy (meV)
(f)
200K INS
600K INS
600K QENS
DOS (meV^{-1})
Energy (meV)

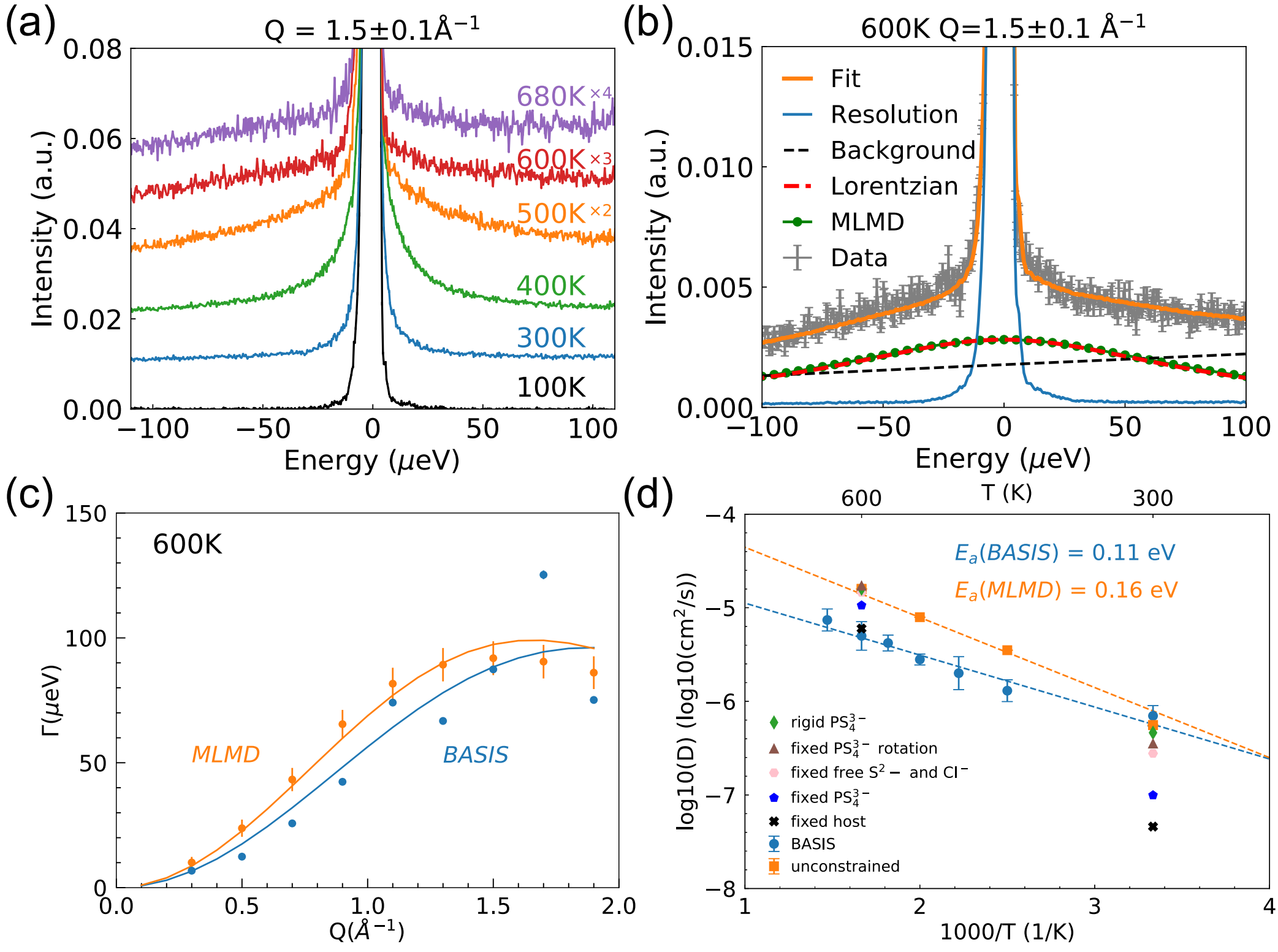
(a)
Q = 1.5±0.1Å^{-1}
Intensity (a.u.)
Energy (μeV)
680K ×4
600K ×3
500K ×2
400K
300K
100K
(b)
600K Q=1.5±0.1 Å^{-1}
Intensity (a.u.)
Energy (μeV)
Fit
Resolution
Background
Lorentzian
MLMD
Data
(c)
600K
Γ(μeV)
Q(Å^{-1})
MLMD
BASIS
(d)
T (K)
600
300
log10(D) (log10(cm^2/s))
1000/T (1/K)
E_a(BASIS) = 0.11 eV
E_a(MLMD) = 0.16 eV
rigid PS_4^{3-}
fixed PS_4^{3-} rotation
fixed free S^{2-} and Cl^-
fixed PS_4^{3-}
fixed host
BASIS
unconstrained

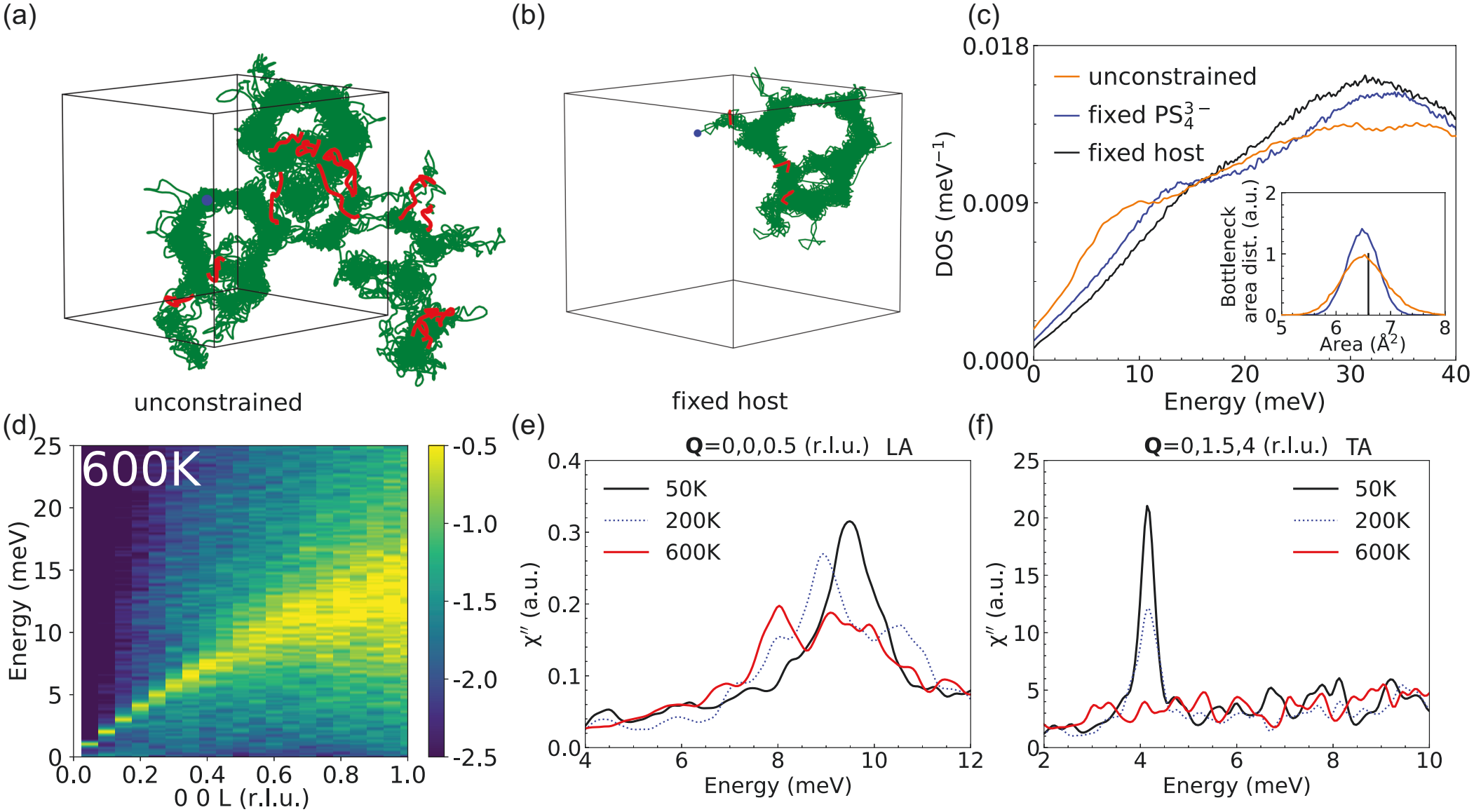
(a)
(b)
(c)
unconstrained
fixed host
0.018
0.009
0.000
DOS (meV^{-1})
unconstrained
fixed PS_4^{3-}
fixed host
Bottleneck area dist. (a.u.)
Area (Å^2)
Energy (meV)
(d)
600K
Energy (meV)
0 0 L (r.l.u.)
(e)
Q=0,0,0.5 (r.l.u.) LA
50K
200K
600K
χ″ (a.u.)
Energy (meV)
(f)
Q=0,1.5,4 (r.l.u.) TA
50K
200K
600K
χ″ (a.u.)
Energy (meV)